

A Virtual Muscle Model of the Arm for EMG-Driven Control of Prostheses

by

Michael F. Fernandez

B.S., Carnegie Mellon University (2020)

Submitted to the Department of Mechanical Engineering
in partial fulfillment of the requirements for the degree of
Master of Science in Mechanical Engineering

at the

MASSACHUSETTS INSTITUTE OF TECHNOLOGY

May 2022

© Massachusetts Institute of Technology 2022. All rights reserved.

Author
Department of Mechanical Engineering
May 6, 2022

Certified by
Hugh M. Herr, Ph.D.
Professor of Media Arts and Sciences
Thesis Supervisor

Certified by
Neville Hogan, Ph.D.
Sun Jae Professor of Mechanical Engineering
Thesis Reader

Accepted by
Nicolas G. Hadjiconstantinou, Ph.D.
Graduate Officer, Department of Mechanical Engineering

A Virtual Muscle Model of the Arm for EMG-Driven Control of Prostheses

by

Michael F. Fernandez

Submitted to the Department of Mechanical Engineering
on May 6, 2022, in partial fulfillment of the
requirements for the degree of
Master of Science in Mechanical Engineering

Abstract

Existing upper extremity prosthesis controllers are unable to provide effective control for persons with amputation, contributing to device abandonment rates as high as 50%. Neuromuscular modeling provides a powerful tool for the development of custom controllers to improve the clinical efficacy of prostheses.

This thesis develops techniques for the creation of models of the arm using a reduced number of virtual muscles. These models take electromyography collected from the residual limb to estimate intended movements for prosthesis control. Neuromuscular model optimization and forward dynamics simulation are used to find parameters that fully define antagonist pairs of virtual muscles that actuate each model degree of freedom. Patient-specific models can be tailored to the morphology of patients with agonist-antagonist myoneural interface (AMI) constructs with minimal hand tuning.

As a case study, a four degree-of-freedom arm model (allowing elbow flexion, index flexion, 3rd to 5th digit flexion, and thumb abduction) was optimized for a subject with unilateral transhumeral amputation who possesses two AMI constructs. The resulting model outputs kinematics that closely match measured kinematics. Joint angle predictions for the elbow, digits, and index finger were very highly correlated with reference trajectories ($r = 0.92$, $r = 0.91$, and $r = 0.87$, respectively), while predictions for the thumb were only moderately correlated ($r = 0.55$). The optimized model also shows the speed-accuracy tradeoff as quantified by Fitts' Law and achieves some degree of graded control.

These results demonstrate how patient-specific neuromuscular models can replicate characteristics of volitional motor control. The highly intuitive control and restoration of native biomechanics granted by such biophysical controllers can allow persons with amputation more independence, raising their quality of life.

Supervisor: Hugh M. Herr, Ph.D., *Professor of Media Arts and Sciences*

Reader: Neville Hogan, Ph.D., *Sun Jae Professor of Mechanical Engineering*

Acknowledgments

I have many people to thank for their support in writing this thesis; it is cliché to say, but I could not have done this without them.

First, I am deeply thankful to Professor Hugh Herr for his research guidance and the opportunity to do exciting work at the cutting edge of bionics. Your vision has inspired me to think bigger, imagine farther, and reach for the impossible.

Innumerable thanks to Professor Neville Hogan, who not only provided valuable feedback on my writing, but also *made the discoveries* that support this work. I aspire to remain passionate about and to contribute to science over a distinguished career like yours.

To Hyun-Geun, Junqing, and Tony: I appreciate your help finding my footing as a graduate student. I've learned much from you all and look forward to continuing our work together.

To all of Biomech, I've enjoyed our coffee breaks, the connections we've built, and even the stress. For some, the lab is only a workplace. For us, it's more.

Thank you to the friends I've made along the way. You've each helped me grow to get to where I am now. To Duncan, thank you for being a great roommate, helping me keep a good work-life balance, and making the graduate school experience more enjoyable.

And to my family - Eric, Gail, Alex, and Caroline - you've given me everything you can and more. My curiosity and love of learning come from you and for that, I'll be forever grateful.

THIS PAGE INTENTIONALLY LEFT BLANK

Contents

1	Introduction	15
1.1	Motivation	15
1.2	Upper Extremity Anatomy	16
1.2.1	The Upper Arm	16
1.2.2	The Forearm	18
1.2.3	The Hand	19
1.3	Upper Extremity Amputation	20
1.3.1	Transradial Amputation	21
1.3.2	Transhumeral Amputation	21
1.3.3	Shortcomings of Traditional Amputation Techniques	22
1.4	Skeletal Muscle Biomechanics	23
1.4.1	Muscle Physiology	24
1.4.2	Muscle Dynamics	24
1.4.3	Hill-Type Muscle Tendon Units	26
1.4.4	Proprioception	28
1.4.5	Neuromuscular Modeling	30
1.5	The Agonist-Antagonist Myoneural Interface	30
1.5.1	Agonist-Antagonist Muscle Dynamics	31
1.5.2	The Agonist-Antagonist Myoneural Interface	33
1.6	Characteristics of Human Movement	35
1.6.1	Muscle Twitch and Tetanus	35
1.6.2	Task Planning and Motion Execution	36

1.6.3	Speed-Accuracy Tradeoff	38
2	Methodology	41
2.1	Data Collection	41
2.1.1	Subjects	41
2.1.2	Electromyography	42
2.1.3	Single Degree of Freedom Kinematic Tasks	43
2.1.4	Kinematic Profile Reconstruction	44
2.2	Neuromuscular Model Generation	45
2.2.1	Model Design	45
2.2.2	Optimization Formulation	47
2.3	Model Validation	51
2.3.1	Trajectory Analysis	51
2.3.2	Muscle Dynamics	51
2.3.3	Fitts' Law	52
2.3.4	Graded Control	53
3	Results	55
3.1	Optimized Neuromuscular Model	55
3.1.1	Optimal Parameter Set	55
3.1.2	Model Muscle Impulse Responses	57
3.2	Demonstration of Natural Biomechanics	57
3.2.1	Fitts' Law Testing	57
3.2.2	Graded Control Tasks	59
3.3	Subject's Comments	66
4	Discussion	71
4.1	Benefits of Biophysical Controllers	71
4.2	Validity of the Simplified Model	72
4.3	Optimal Muscle Parameters	74
4.4	Replication of Native Biomechanics	77

4.4.1	Speed-Accuracy Tradeoff	77
4.4.2	Graded Control Tasks	78
4.5	Contributions	80
4.6	Future Directions	80
A	Supplementary Figures	83

THIS PAGE INTENTIONALLY LEFT BLANK

List of Figures

1-1	Musculature of the Upper Arm	17
1-2	Musculature of the Forearm	19
1-3	Intrinsic Musculature of the Hand	20
1-4	Demonstration of Transradial Amputation Technique	22
1-5	Sarcomere Structure	25
1-6	Normalized Muscle Force Relationships	26
1-7	Hill-type 3 Element Muscle-Tendon Unit	27
1-8	Muscle Spindle Fiber Morphology	29
1-9	Golgi Tendon Organ Morphology	30
1-10	Model of agonist-antagonist muscle configuration	32
1-11	Residual limb morphology for a person with AMI constructs	34
1-12	Muscle Twitch and Tetanus	36
2-1	Model of Virtual Joint with Agonist-antagonist Actuation	46
2-2	Optimization Input Data	48
3-1	Optimal Model Trajectories	58
3-2	Impulse Responses	59
3-3	Fitts' Law Testing for Model Elbow	60
3-4	Fitts' Law Testing for Model Digits	61
3-5	Fitts' Law Testing for Model Thumb	62
3-6	Fitts' Law Testing for Model Index	63
3-7	Fitts' Law Linear Regression	64
3-8	Graded Control Tasks	65

3-9	Mean Virtual Joint Positions During Graded Control Tasks	67
3-10	Graded Control Task Directional Correctness	68
A-1	Full Elbow Graded Control Trajectory	84
A-2	Full Digits Graded Control Trajectory	85
A-3	Full Thumb Graded Control Trajectory	86
A-4	Full Index Graded Control Trajectory	87

List of Tables

2.1	EMG Electrode Placement	43
2.2	Fixed Physiological Parameters for four Degree of Freedom Model	47
2.3	Bounds on Physiological Decision Variables	50
3.1	Optimized Muscle Parameters	56
3.2	Optimized EMG Weighting Matrix	56
3.3	Dimensionless Log Jerk from Reference and Optimized Trajectories	57
3.4	Impulse Response Peak Amplitudes and Times	57
3.5	Indices of Performance from Fitts' Law Testing	59
3.6	Pairwise p -values for Differences between Model Outputs during Graded Control Tasks	69

THIS PAGE INTENTIONALLY LEFT BLANK

Chapter 1

Introduction

This chapter introduces the background on skeletal muscle physiology, advanced amputation procedures, muscle modeling and control of volitional movement in humans necessary to support the work presented in this thesis. The information is drawn from existing published work and ongoing research performed by the Biomechatronics group in the MIT Media Lab.

1.1 Motivation

The world has been designed considering individuals with two arms and two legs. Limb loss, therefore, hampers a person's engagement in activities of daily living. Persons missing hands, the finest tools evolution has created, are limited in their ability to handle tools and manipulate objects. Existing prosthetic devices are unable to replicate the dexterity provided by the biological arm's 30 degrees of freedom - the most advanced limbs have fewer than 20 controllable degrees of freedom (DoF) [1], though more common commercially available devices are often limited to one or two. This results in complaints about the comfort, cognitive burden during use, and functionality of available devices, which leads to device abandonment. Estimates vary by amputation level, but the literature suggests that at least 30% to 50% of users do not regularly use their prosthesis [2].

Improvements in robotics technology will result in prosthetic arms with the ap-

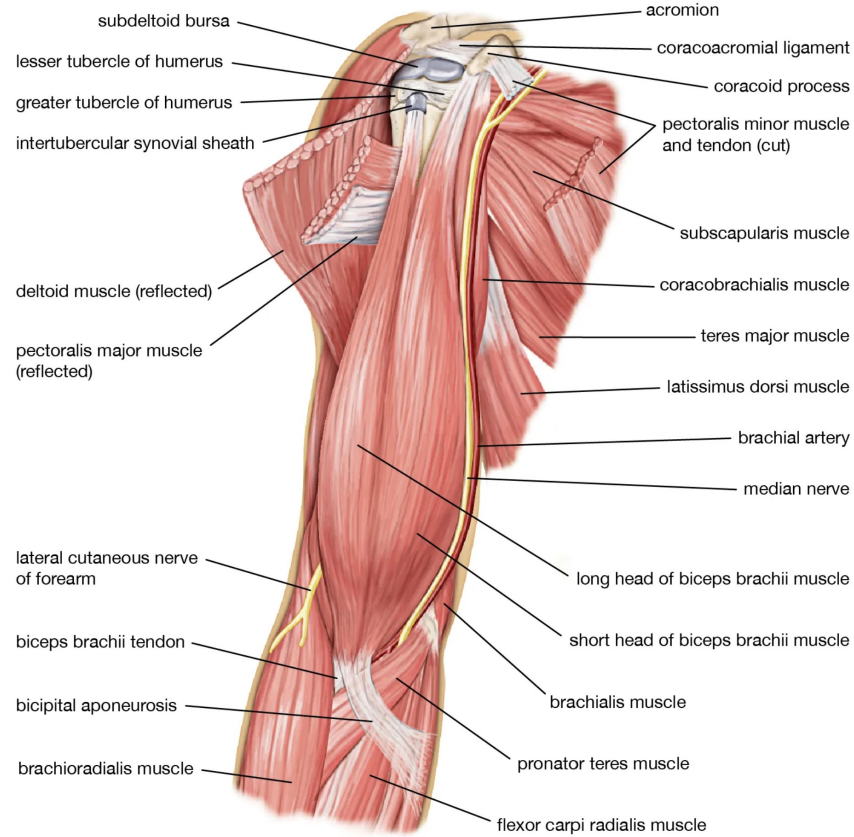
proximate form factor of a biological limb within the next decade. These devices will provide multiple degrees of freedom for movement, but control algorithms that allow truly intuitive, simultaneous, and proportional control have not been deployed outside controlled laboratory settings. To restore lost functionality, it is informative to leverage millions of years of evolution, by looking to native limb dynamics. Such bio-inspired controllers integrate well with the body's existing control systems and take advantage of biological signals that are still available. In addition, controllers employing biophysical models avoid long training periods that require a user to learn how to refer contraction of certain residual muscles to control other joints. Thus, improved prosthetic controllers can increase the utility of a prosthetic device, decrease rates of abandonment, and grant greater independence to those with amputations.

1.2 Upper Extremity Anatomy

The arm is a very complicated structure; it consists of dozens of bones, muscles, and nerves that must function in a coordinated manner to allow persons to interact with the world. With such complexity, it is not surprising that the arm and especially the hand have oversized representations within the cortical homunculus [3]. The function of the biological limb must be understood before other morphologies can be considered. The human arm is divided into three main compartments: the upper arm, the forearm, and the hand. The anatomy of each section will be discussed briefly, in turn.

1.2.1 The Upper Arm

The upper arm spans between the shoulder girdle and the elbow joint. It contains one bone, the humerus, which serves as the origin and insertion of muscles within the upper arm. The humerus connects to the body at the glenohumeral joint, which is a multi-axis shallow ball and socket that enables the extensive range of motion of the arm. The primary actuators of the upper arm are the deltoid muscles, which flex, extend, and abduct the upper arm. Also spanning the glenohumeral joint are



© Encyclopædia Britannica, Inc.

Figure 1-1: Musculature of the Upper Arm [4]

the rotator cuff muscles - the supraspinatus, the infraspinatus, the teres minor, and the subscapularis. These muscles all insert along the humerus. Muscles that move the forearm originate in the upper arm. The elbow consists of three joints, but is often treated as a single hinge joint. The elbow flexors are the biceps brachii and the brachialis. The muscle that extends the elbow is the triceps brachii. The musculocutaneous nerve is the primary motor innervation for elbow flexors and provides sensory innervation for skin on the lateral portion of the forearm. The radial nerve innervates the triceps brachii. An anatomical drawing of the musculature of the upper arm is shown in Figure 1-1.

1.2.2 The Forearm

Distal to the elbow joints is the forearm, which contains the muscles that move the wrist and the extrinsic muscles of the hand. This section of the arm contains 20 muscles, contributing greatly to fine control of the hand. There are two major bones in the forearm: the radius and the ulna. The ulna is medial to the radius at the elbow joint, but these bones evolved to slide past each other to allow a motion that only occurs at the upper extremity, pronation and supination. These movements are controlled by the pronator and the supinator muscles, which originate on the radius and ulna and insert on the ulna and radius, respectively. Wrist flexion is primarily achieved by the flexor carpi ulnaris and radialis, which lie in the anterior compartment of the forearm. The wrist is extended using the extensor carpi ulnaris, extensor carpi radialis longus, and the extensor carpi radialis brevis, which lie in the posterior compartment of the forearm.

The extrinsic muscles of the hand also originate in the forearm. The flexor digitorum superficialis and the flexor digitorum profundus are muscles in the anterior forearm that each split into four tendons that pass through the carpal tunnel to individually flex the fingers. On the other side of the forearm, in the posterior compartment, are the finger extensors - the extensor digitorum communis, the extensor indicis, and the extensor digiti minimi. The tendons from these muscles pass under the extensor retinaculum, a band of fascia that runs across the back of the wrist, to extend the fingers. Some thumb muscles are contained within the forearm; these include the abductor pollicis, the extensor pollicis longus, and the extensor pollicis brevis. The extrinsic muscles of the hand are all multiarticular, so they contribute to movements of the wrist as well.

Motor innervation for muscles on the anterior forearm (flexor and pronator muscles) of the forearm generally comes from the median and ulnar nerves. Motor innervation for the extensor and supinator muscles generally comes from the radial nerve. Sensory innervation is provided by the antebrachial cutaneous nerves. However, there is variability in the specifics of sensory and motor innervation, to the degree that the

number of muscles and tendons in the forearm are not the same in all people. Figure 1-2 shows the musculature of the anterior and posterior components of the forearm.

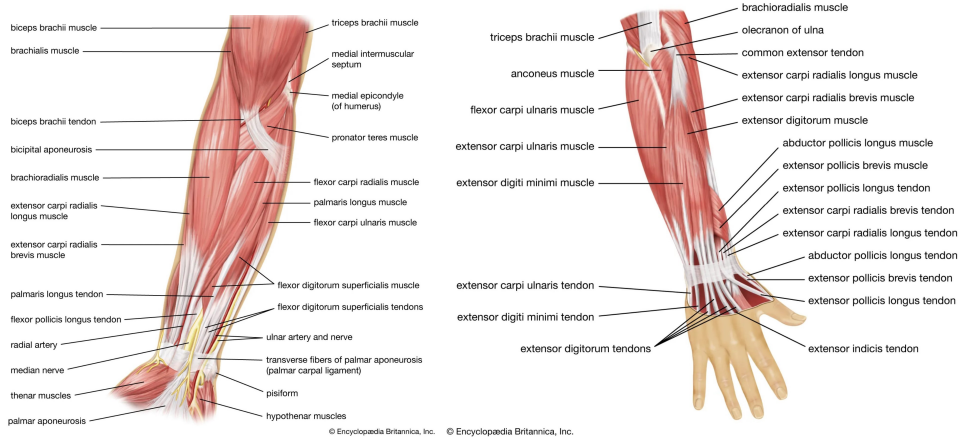


Figure 1-2: Musculature of the anterior (left) and posterior (right) compartments of the forearm [5] [6]

1.2.3 The Hand

The hand is among the most complex structures of the human body. It has over 20 bones, 20 joints, and 30 muscles working in concert. Without precise control over so many structures, it would not be possible to type out this thesis. It is with our hands, and especially due to the opposable thumb, that humans have built tools that enable modern technological society. Each digit consists of four joints: the carpometacarpal joint at the base of the hand, the metacarpophalangeal joint where the palm meets the finger, and the proximal and distal interphalangeal joints along the finger. In addition to the extrinsic hand muscles found in the forearm, the fingers are also actuated by intrinsic muscles of the hand. The lumbricals assist in digit flexion; the palmar interossei adduct the fingers, flex the metacarpophalangeal joints and extend the interphalangeal joints; the dorsal interossei abduct the fingers. Many of the muscles that move the thumb originate within the hand, often near the wrist, inserting on the proximal or distal joints of the thumb. The flexor pollicis brevis, abductor and adductor pollici, and opponens pollicis allow the thumb to move along both its axes of movement. The intrinsic muscles of the hand are innervated by the

median and ulnar nerves for both motor control and sensory perception. See Figure 1-3 for a representation of musculature in the hand.

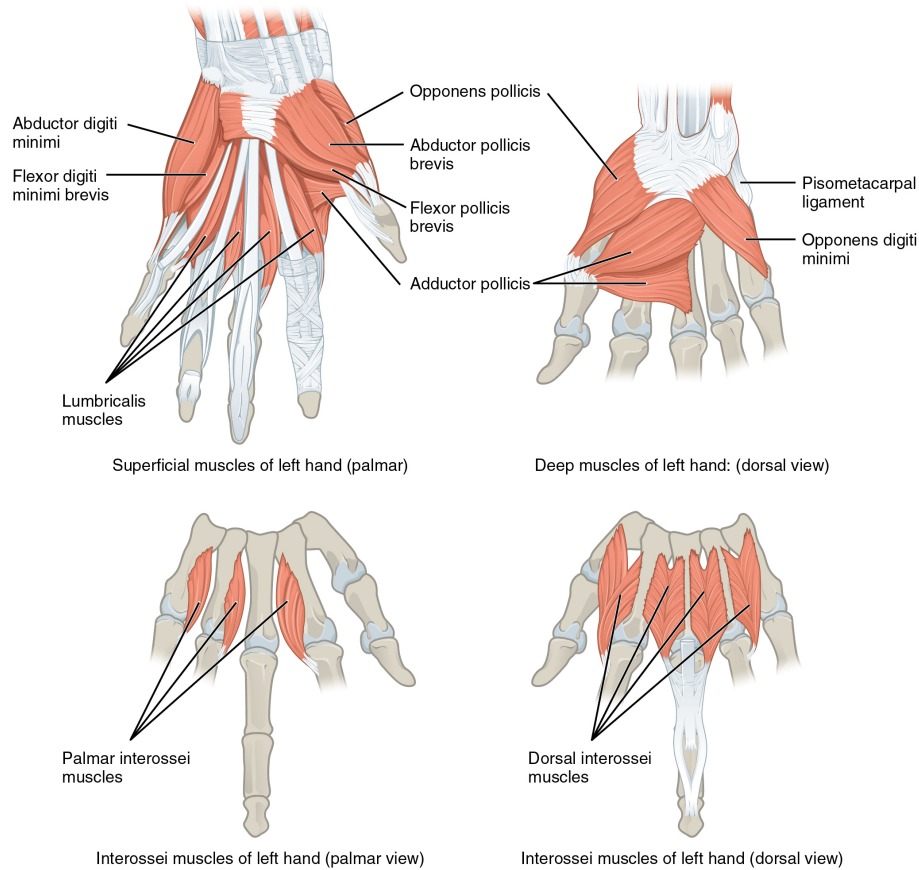


Figure 1-3: Intrinsic Musculature of the Hand [7]

1.3 Upper Extremity Amputation

When the function of the arm is impaired and the limb cannot be salvaged, an amputation is performed. Upper extremity amputations most commonly take place following traumatic injury, but are also performed for treatment of peripheral vessel diseases or diabetes. 80% of upper extremity amputations are acquired traumatically, whether acutely or following elective surgery [8]. Amputations are named according to their level. From most distal and in ascending order, major categories of arm amputation include transcarpal at the wrist, transradial through the forearm, and transthumeral

at the upper arm. Upper extremity amputation can be performed through the joints as well. It is typically desired to preserve as much of the native anatomy as is healthy, though depending on the indications for amputation, this may not always be possible. Further, commercial prostheses expect limb segments to be of certain lengths such that the profile of the arm when a device is worn matches that of the biological limb. An explanation of standard amputation techniques precedes the exploration of modern advances in upper extremity amputation.

1.3.1 Transradial Amputation

Transradial amputation is limb removal between the elbow and wrist, cutting through the radius and the ulna. Preserving the length of the forearm improves functional outcomes; the longer the remaining limb segment, the greater the degree of pronation and supination that is possible. For prosthetic fitting, saving more than 4 cm of the ulna is preferable. Under sterile conditions, two incisions are made along the anterior and posterior forearm at the intended level of bone sectioning. These skin flaps should be made equal to half the diameter of the forearm at the amputation level so that they will be able to close over the resected tissue. The nerves are transected proximal to the amputation level so they can retract high within the residual limb. The radius and ulna are cut and rasped to keep their surfaces smooth. Next, the muscle bellies are cut, leaving the deep flexor digitorum muscle long so it can be brought across the end of the transected bones and sutured to the deep fascia on the posterior side of the arm. Thus, the shortened muscles are affixed isometrically to be used as padding within a prosthetic socket [8], though much of the forearm is avascular tissue that provides poor padding at the end of the residuum. Finally, the skin flaps are stitched together to close the wound as shown in Figure 1-4.

1.3.2 Transhumeral Amputation

When all tissue up to the elbow joint is unsalvageable, a person is indicated for a transhumeral amputation. During this procedure, the hand, forearm, and elbow joint

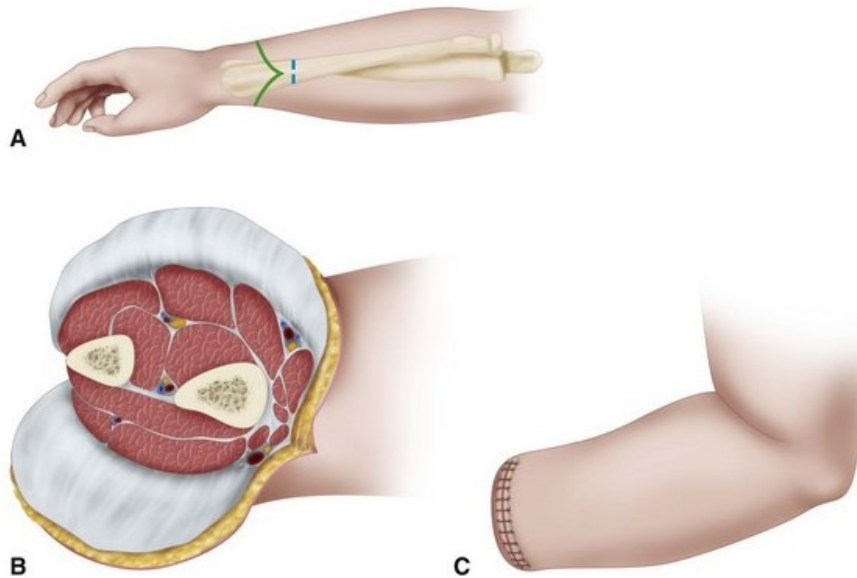


Figure 1-4: Demonstration of transradial amputation technique, including the location of the incisions, resection of muscle and bone, and suturing of skin flaps. [9]

are removed. The amputation techniques are similar to those at the transradial level. Two incisions are made roughly 4 cm proximal to the elbow joint, creating an anterior and a posterior flap. This level is chosen such that prosthetic elbow joint appears equal to the biological elbow location. The posterior flap is left longer, typically twice the length of the anterior flap, so that it can be used to pad the end of the humerus. The biceps and brachialis muscle bellies are cut and the muscles are allowed to retract proximal to the amputation level. The median, ulnar, and radial nerves are transected and retract into the proximal wound as well. The humerus is cut and smoothed to prevent spurs. As in the transradial case, the posterior flap, consisting of the triceps brachii, is transposed anteriorly and sutured to the deep fascia of the upper arm. This creates padding that prevents the end of the humerus from breaking through the skin. As a result, the muscles can only contract isometrically following transhumeral amputation [8].

1.3.3 Shortcomings of Traditional Amputation Techniques

Amputation is often considered a last resort and follows other attempts to salvage a limb. This does make sense; any level of upper extremity amputation would reduce

a person's dexterity. Even when necessary, traditional amputation techniques leave much to be desired.

Best known among the shortcomings is the 'phantom limb' syndrome - the sensation of pain or movement within the missing limb. Though the mechanism behind it is unknown, this condition can be painful. The phantom limb may feel stuck in an uncomfortable position or it can feel as it moves as the amputee contracts their residual musculature. However, the sensation does not always correspond to the intentions of the amputee, likely due to the absence of afferents from mechanoreceptors in the muscles. Proprioception is necessary for the proper regulation of movement and maintenance of the body's internal postural model, especially with regard to joint position estimation [10]. In addition to phantom limb pain, benign masses of soft tissue and nerves may form as the nervous tissue remodels. These neuromas can be extremely painful. At present, neuropathic pain following amputation is treated with nerve blocks or pain medication, neither of which are feasible long-term management strategies.

Barring these painful conditions, the isometric fixure of muscles in the residuum limits their usefulness for prosthesis control. The loss of muscle strain, as well as the loss of entire muscles, interrupts stereotypical muscle activation patterns; these interfere with dynamic motion primitives that are known to reduce the cognitive load required to execute movement [11]. Most myoelectric prostheses must then rely on pattern recognition techniques to distinguish between desired movements. Given that socket placement, fatigue, and other environmental conditions impact the consistency of electromyographic readings, robust pattern recognition requires that only a limited number of movements be trained.

1.4 Skeletal Muscle Biomechanics

To design a biomimetic controller, native muscle function must be known. The following section details how muscle physiology determines muscle function and resulting mathematical models of muscle.

1.4.1 Muscle Physiology

Skeletal muscles are the actuators of the body. At the simplest level, they can be imagined as ropes knotted around the bones they move as they are only able to pull. The basic contractile unit of skeletal muscle is the sarcomere, which consists of two types of overlapping protein filaments. A sarcomere in the relaxed and contracted states is shown in Figure 1-5. When muscles contract, the thick myosin filaments slide past the thin actin filaments, shortening the sarcomere and producing force. This is termed the sliding filament model of muscle contraction [12].

According to this model, when muscles are commanded to contract, the heads of myosin fibers bind to actin filaments as part of the cross-bridge cycle. This is an active process that consumes adenosine triphosphate (ATP), which is why muscles fatigue after sustained contraction. Myosin hydrolyses an attached ATP molecule to undergo a conformational change that cocks its head. The head then attaches to a binding site on the actin filament, releasing adenosine diphosphate (ADP) and an inorganic phosphate to initiate the 'power stroke'. During the power stroke, the cocked myosin head pivots towards the center of the sarcomere, pulling the filaments past each other to shorten the sarcomere. Binding of a new molecule of ATP to the myosin head detaches it from the actin filament, restarting the cycle.

Though Figure 1-5 shows a planar representation, sarcomeres are three-dimensional structures. Actin and myosin filaments are arranged hexagonally when viewed axially - the myosin heads can attach to actin on all sides. In addition, there are many sarcomeres arranged in series within each myofibril. It is the combined action of many sarcomeres in series and many myofibrils in parallel that lead to the macroscopic force production and length changes observed when muscles contract.

1.4.2 Muscle Dynamics

The mechanism of muscle contraction has concrete consequences for muscle dynamics. First, there is a relationship between the length of the muscle and the force the muscle can produce. When a muscle is relaxed, there is overlap between the actin and

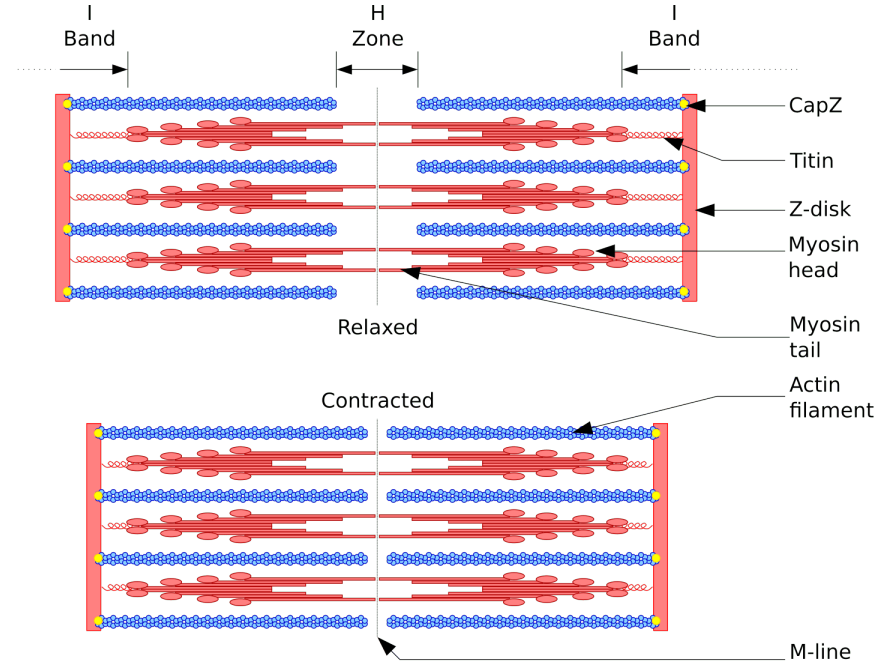


Figure 1-5: Sarcomere anatomy, showing the change in actin and myosin fiber overlap in the relaxed and contracted states [13]

myosin filaments; as the muscle contracts, this overlap increases, more cross-bridges form, and the muscle can contract with greater force. The force increases until the end of the myosin filament reaches the I-bands. From this point on, the force decreases with additional contraction. Similarly, the force decreases with extension beyond the rest length because the overlap decreases. This defines the sarcomere's active force-length curve; *in vivo*, the sarcomere would produce zero force at lengths below 1 micron and above 3.5 microns, with peak force at 2.2-2.3 microns. Contraction and extension is common to all sarcomeres within the muscle, so the shape of the muscle-level force-length curve matches that of individual sarcomeres.

There is also a relationship between the velocity of muscle contraction and the force produced. The likelihood that any given cross-bridge forms decreases as muscle shortening velocity increases because it takes time for the filaments to bind. Thus, the force produced decreases from the maximum isometric force, at zero velocity, to zero at some maximum contraction velocity. The behavior holds for muscle lengthening as well, with force increasing beyond the isometric maximum as the muscle

stretches. Physiologist A.V. Hill's work on the thermodynamics of shortening muscle demonstrated that this force-velocity relationship is hyperbolic [14]. Each of the active force-length and force-velocity relationships scale linearly with the level of muscle activation.

Other tissues in muscle contribute to the net force produced as well. There is elasticity in the fascia, ligaments, and muscle tissue itself that produces a restoring force as the muscle stretches beyond its rest length. This force increases nonlinearly with muscle stretching and defines the passive force-length curve. In addition, tendons connect each muscle to the skeletal system. Tendons also have a nonlinear force-length relationship where the restoring force produced increases with strain and is zero when the tendon is slack. These relationships are visualized in Figure 1-6 using normalized lengths, forces, and velocities. The active and passive force-length relationships are additive, with both seen in the first plot. The normalization allows these curves to be applied to various muscles given their optimal fiber length, tendon slack length, maximum isometric force, and maximum contraction velocity.

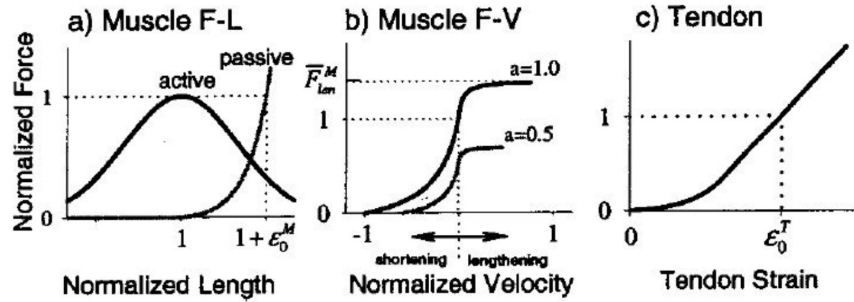


Figure 1-6: Normalized force relationships for muscle, showing the active and passive force-length curves, the force-velocity curve, and the tendon force-length curve. Reproduced with permission from the ASME [15]

1.4.3 Hill-Type Muscle Tendon Units

With an understanding of this behavior, A.V. Hill put forth a mathematical model of muscle-tendon units (MTUs) that captures the dynamics of real muscles in the 1930's [14]. The most common form of the Hill muscle model is the three-element model,

which uses mechanical analogues to reproduce observed muscle dynamics. The active force production is captured by a force generator, termed the contractile element (CE), that produces a force scaled by the muscle activation according to the force-length and force-velocity curves for a given muscle. The force generator is in parallel with a spring, termed the parallel element (PE), that simulates the elastic properties of muscle tissue. Finally there is the series element (SE), which represents the tendon. Often, the pennation angle between the muscle and the tendon is included to further generalize the model. A mechanical diagram of the three-element model is included in Figure 1-7. Such a model is competent to describe the dynamic behavior of muscle, including the linear relationship between muscle force and stiffness [16].

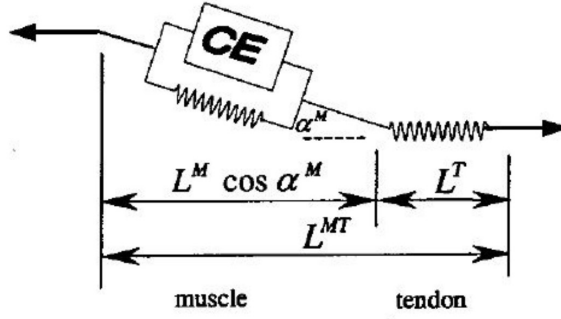


Figure 1-7: Mechanical diagram of a Hill-type 3 element muscle-tendon unit, showing the contractile, series elastic, and parallel elastic elements. Reproduced with permission from the ASME [15]

Performing a force balance at the muscle-tendon junction allows a differential equation to be written for the MTU:

$$f_{iso}(a(t)f_{AL}(l^M)f_v(\dot{l}^M) + f_{PL}(l^M)) \cos(\alpha) - f_{iso}f_{SE}(l^T) = 0 \quad (1.1)$$

where f_{iso} is the maximum isometric force the muscle can produce, $a(t)$ is the muscle activation at a given time, α is the pennation angle, l^M is the muscle length and l^T is the tendon length (such that MTU length $l^{MT} = l^M \cos(\alpha) + l^T$), $f_{AL}(l^M)$ and $f_{PL}(l^M)$ are the force generated at the muscle's current length according to its active and passive force-length curves, respectively, $f_v(\dot{l}^M)$ is the force generated according to the force-velocity curve, and $f_{SE}(l^T)$ is the force in the tendon according to its

force-length curve.

1.4.4 Proprioception

Precise control of movement relies on the body's ability to know the position of each joint in space. This sense is called proprioception and is mediated by native receptors within muscles. The sensors generate afferent nerve signals that carry information about muscle states to the brain. Two main types of receptors provide proprioception: muscle spindles and Golgi tendon organs.

Muscle spindles are stretch receptors that form the intrafusal muscle fibers, running parallel to the main extrafusal muscle fibers within the muscle belly. These intrafusal fibers are wrapped in spirals by sensory neurons. As a muscle stretches, the spiral of the neurons changes shape, opening mechanically gated ion channels and triggering action potentials. In this way, muscle spindles are able to signal muscle movement. There are three types of intrafusal fibers - dynamic nuclear bag fibers, static nuclear bag fibers, and nuclear chain fibers. Nuclear bag fibers are named for their fusiform shape. Static nuclear bag fibers are wrapped by type Ia and type II sensory neurons, while dynamic nuclear bag fibers are wrapped only by type Ia sensory neurons. Nuclear chain fibers are wrapped by both types of sensory neurons. These neurons exhibit different firing patterns as a muscle is stretched. Type Ia fibers demonstrate increased firing rates as the muscle is stretched more rapidly, a phenomenon called dynamic sensitivity. Type II fibers do not have dynamic sensitivity and fire at a consistent rate for a given muscle length. In this way, type Ia and type II fibers can continuously measure both the length and the velocity of a muscle.

These are active sensors as motoneurons innervate some of the intrafusal muscle fibers. Dynamic γ -motoneurons innervate the dynamic nuclear bag fibers and static γ -motoneurons innervate the static nuclear bag and nuclear chain fibers. These motoneurons modulate the sensitivity of the muscle spindle by adjusting the tension in the intrafusal fibers, which are contractile only at their ends. The three types of intrafusal fibers and their innervations can be seen in Figure 1-8. Muscle spindles participate in the spinal stretch reflex by triggering contraction to oppose unexpected

rapid stretching in the muscle.

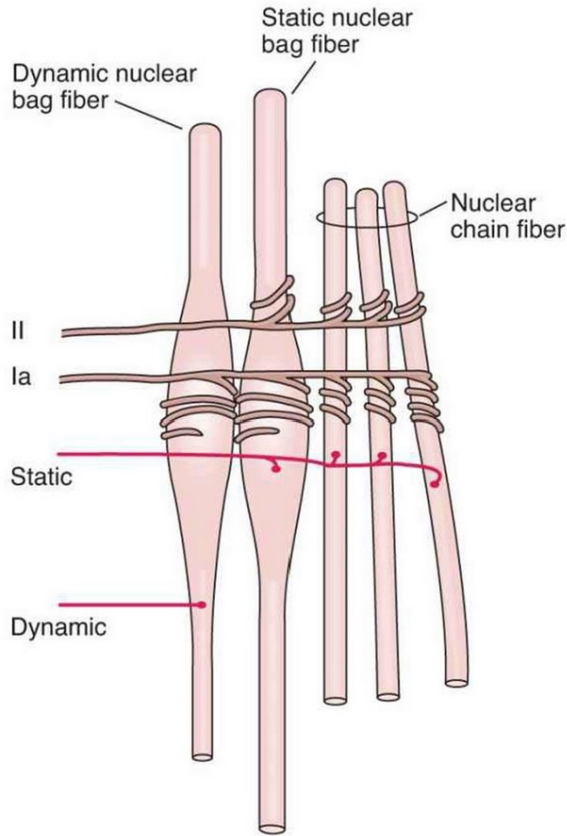


Figure 1-8: Muscle Spindle Fibers and their Sensory and Motor Innervation [17]

Golgi tendon organs, as shown in Figure 1-9, lie in series with the muscle, in the musculotendinous junction between the muscle fibers and the tendon. They do not have motor innervation and are innervated by type Ib sensory neurons, which weave through the extrafusal muscle fibers at the muscle-tendon junction. As the muscle comes under load, either externally or during contraction, the extrafusal fibers compress and deform, which opens gated ion channels in the Ib afferent axons. This triggers action potentials whose frequency depends on the magnitude of the load, which allows Golgi tendon organs to indicate muscle force. In this way, Golgi tendon organs participate in feedback loops that regulate the intensity of muscle contraction.

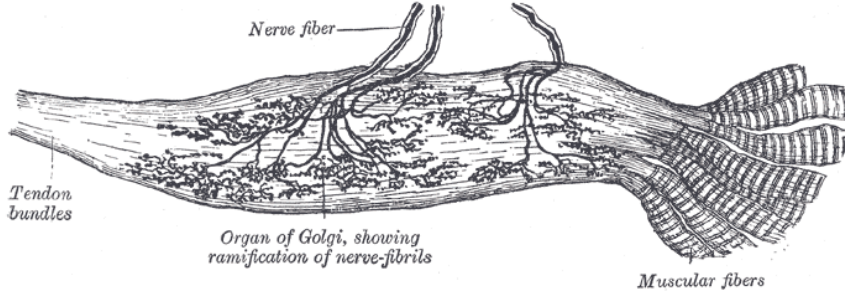


Figure 1-9: Golgi tendon organ showing musculotendinous junction and sensory innervation [18]

1.4.5 Neuromuscular Modeling

With equation 1.1, muscle contractions can be simulated. Typically, the muscle force-velocity relationship is inverted. This yields

$$\dot{l}^M = f_v^{-1} \left\{ \frac{\frac{f_{SE}(l^T)}{\cos(\alpha)} - f_{PL}(l^M)}{a(t)f_{AL}(l^M)} \right\} \quad (1.2)$$

noting that the force-velocity curve is a hyperbola, which is invertible. An equation in this form can be numerically integrated to calculate the muscle length in response to a time-varying muscle activation input.

To define a neuromuscular model, the specific force-length, force-velocity, and tendon force-length curves must be found. There are a number of parameterizations that are commonly used - the Thelen model [15], the van Soest and Bobbert model [19], the Shadmehr-Arbib model [16], or the Kaplan-Silva model [20]. Once a model is selected, an optimization procedure is usually used to fit model parameters to physiological data. Details for multi-muscle modeling follow.

1.5 The Agonist-Antagonist Myoneural Interface

Studying the behavior of single muscles is instructive as an exercise, but does little to inform an understanding of multi-joint limb movements. For that, multiple muscles, their coordination, and sensory feedback must be considered.

1.5.1 Agonist-Antagonist Muscle Dynamics

Within the body, muscles must come in pairs because they are unidirectional actuators. These are termed agonist-antagonist muscle pairs. Muscles, which pull linearly, insert on a bone a certain distance from the joint's axis of rotation, actuating the bones as levers. When the muscle contracts, the muscle force is multiplied by the moment arm to create a torque about the joint. The torques from multiple muscles at a joint sum, producing a net muscular torque given as

$$\tau(\theta, t) = \sum_i r_i(\theta) F_i(\theta, t) \quad (1.3)$$

where $\tau(\theta, t)$ is the net muscular torque, i indexes all muscles acting on the joint, θ is the joint angle, $r_i(\theta)$ is the angle dependent moment arm of muscle i , and $F_i(\theta, t)$ is the angle dependent force produced by muscle i at time t . Note that, in contrast to the definition given above, the muscle force is given in terms of joint angle rather than MTU length. This formulation demonstrates that the MTU length can be calculated from the joint angle and knowledge about the locations of muscle origins and insertions.

If the limb is considered an open kinematic chain, then the forward kinematic equations give the configuration-dependent location of the end effector. Differentiating these equations defines a kinematic Jacobian. Via the principle of virtual work, it can be shown that

$$\tau = \mathbf{J}^T F \quad (1.4)$$

where τ is the vector of torques for each joint, \mathbf{J} is the kinematic Jacobian relating changes in configuration to motion of the endpoint, and F is the vector of applied forces. Equating equations 1.3 and 1.4 for the case of a single uniarticular muscle shows that the moment arm is calculated as

$$r(\theta) = \frac{dl^{MT}(\theta)}{d\theta} \quad (1.5)$$

after substituting for the single link Jacobian.

Other tissues - fascia, ligaments, joint capsules - can be lumped into single joint stiffness and joint damping parameters that contribute to the net torque at the joint. External loads, including gravity and contact forces, are summed to be included as well. All together, Newton's second law shows that motion about a single joint would be described by

$$I\ddot{\theta} = \sum_i r_i(\theta)F_i(\theta) - K(\theta - \theta_0) - B\dot{\theta} + \sum_j \tau_j \quad (1.6)$$

where I is the limb inertia about the axis of rotation, K is the lumped joint stiffness, B is the lumped joint damping, θ_0 is the joint's position when muscles are at their rest lengths, and τ_j are the j applied external torques. Other terms are defined as in equation 1.3. This equation is sufficient to fully describe the joint kinetics. Figure 1-10 shows a representative linear model of an antagonist pair of Hill-type muscles whose dynamics would be described according to equation 1.6.

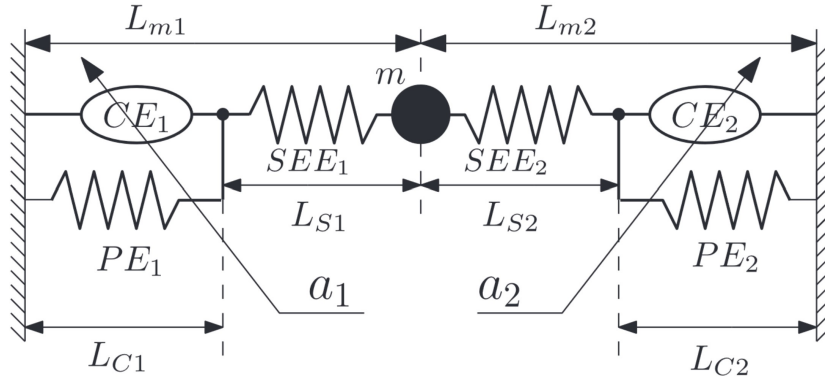


Figure 1-10: Two Hill-type muscles actuating a point mass in an agonist-antagonist configuration [21]

This framework can be expanded to cover multiple joints through the use of inertia, stiffness, and damping tensors. It becomes necessary to treat a full limb as a kinematic chain with configuration dependent rather than constant matrices. Consider, for example, shoulder flexion - if the elbow is fully extended, the effective inertia seen by the shoulder is much larger than if the elbow is flexed. In standard form, the dynamic

equation governing the motion of a full limb is

$$I(\theta)\ddot{\Theta} + B(\theta, \dot{\theta})\dot{\Theta} + K(\theta)\Theta + \sum_i r_i(\theta)F_i(\theta) = \sum_j \tau_j \quad (1.7)$$

where Θ is the vector of joint angles, $I(\theta)$ is the configuration dependent inertia tensor, $B(\theta)$ is the configuration dependent damping, $K(\theta)$ is the configuration dependent stiffness. This equation can be numerically integrated to find trajectories for each joint of the limb.

1.5.2 The Agonist-Antagonist Myoneural Interface

The agonist-antagonist myoneural interface (AMI) is a novel construct under investigation for the preservation of proprioception in persons with amputation. During the surgical procedure, the distal ends of two naturally antagonistic muscles are mechanically linked in series with a piece of tendon passed through a synovial canal [22]. In essence, a biological pulley is built in the residual limb. This linkage restores native agonist-antagonist dynamics: when one muscle of the pair is stimulated to contract, the antagonist muscle is stretched. The physiologically relevant strain activates the muscle spindles and Golgi tendon organs in the construct, generating sensory afferents as observed in the intact limb.

Electromyographic signals can be read from the constructs and used in the forward control path for robotic prosthesis as proprioceptive feedback simultaneously signals muscle states. Studies of the AMI in subjects with lower extremity amputation has demonstrated how recipients can use this feedback from their construct to better control an active prosthetic in a biomimetic manner. For example, the subtalar joint of a 2-DoF prosthetic ankle everts naturally when approaching an obstacle when controlled by an AMI subject but does not when controlled by a person with traditional transtibial amputation [23].

The construct was developed to allow bidirectional neural communication with an active prosthetic. With functional electrical stimulation (FES), it's possible to initiate contraction of one muscle and stretching of its antagonist in response to external

events. Evidence suggests that graded amplitude FES in response to force applied to the prosthetic device can provide graded force feedback used by the participant to modulate muscle activity. Thus, the AMI is a promising approach to close the feedback loop for improved active control of robotic prostheses. How AMI constructs can be made in the residuum is shown in Figure 1-11, where two constructs are seen in the residual limb of a person with transtibial amputation.

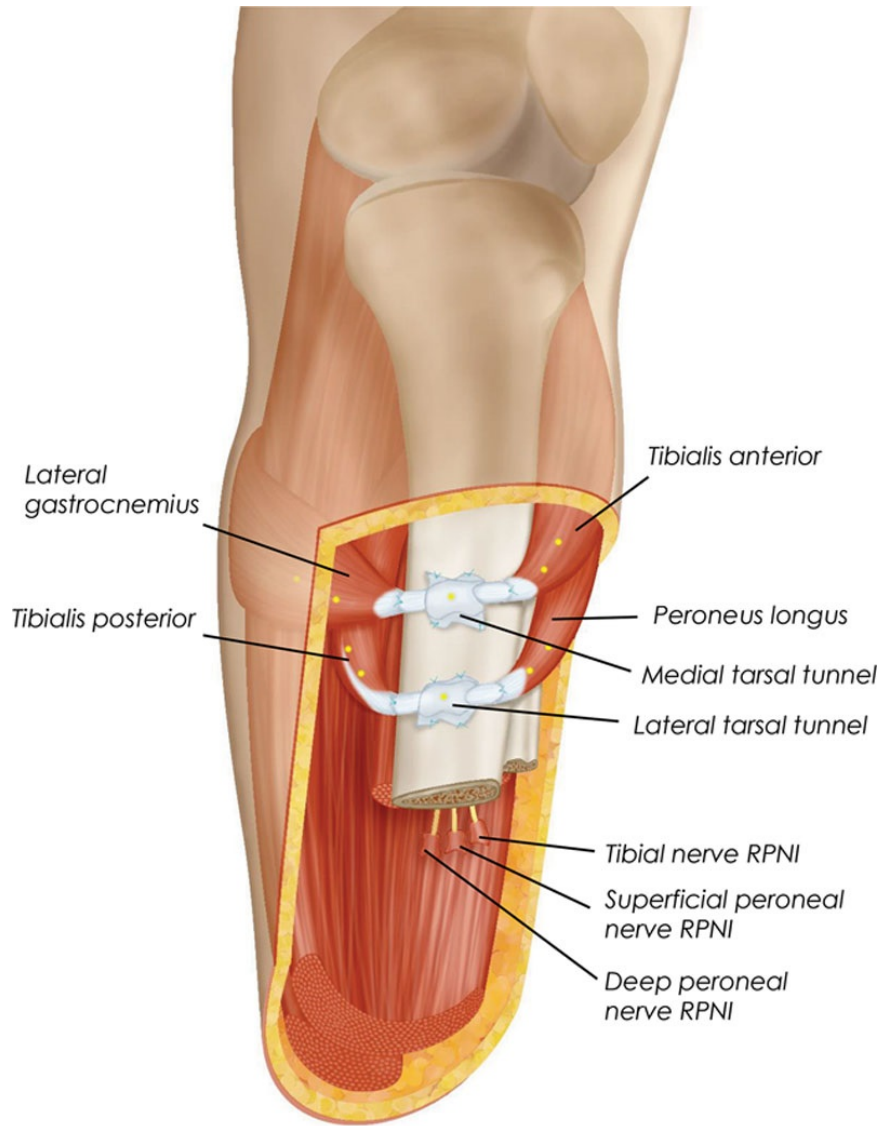


Figure 1-11: The construction of two AMI pairs following transtibial amputation. One pair can primarily control dorsi- and plantarflexion; the other can control ankle inversion-eversion. Regenerative peripheral nerve interfaces (rPNIs) are built for other nerve endings [24]

1.6 Characteristics of Human Movement

Through all its complexity, certain characteristics of volitional human movement appear invariant. Study of motor tasks at different scales and for different parts of the body has motivated theories about movement and task planning that have both predictive and explanatory power.

1.6.1 Muscle Twitch and Tetanus

At the base of all theories of human motor control is the physiology of the musculoskeletal system. Muscle contraction occurs following depolarization due to an action potential in a motoneuron. Depolarization opens calcium channels in the sarcoplasmic reticulum, increasing the concentration of calcium ions in the intracellular space. These ions bind to troponin fibers in the sarcomeres, causing confromational changes that allow the muscle to contract according to the sliding filament model. Thus, following a short latency period, the force in the muscle grows. After depolarization, the channels close and calcium ions are pumped out of the intracellular space, so contraction ceases and force begins to decrease again. The rates of force increase and decrease are governed by two different time constants: the activation time constant measures the binding of calcium to troponin and the deactivation time constant shows the rate of calcium reuptake into the sarcoplasmic reticulum. These processes are rapid enough that the muscle does not contract to maximum force following a single action potential. The response to one action potential is deemed a muscle twitch.

Muscle twitches can sum when a train of action potentials cause successive depolarizations. This increases the force in the muscle until the maximum force is reached and force production plateaus. This is termed tetanic contraction and occurs at different stimulation frequencies depending on the makeup of a muscle, but occurs above 60 Hz in most muscles. If the rate of arrival of action potentials increases further, unfused tetanic contraction becomes fused tetanic contraction and the force output of the muscle remains constant. Figure 1-12 shows muscle twitches, summation, and

tetanus. This shape - increasing force during the contraction period and decreasing force during the relaxation period - is observed in all skeletal muscles.

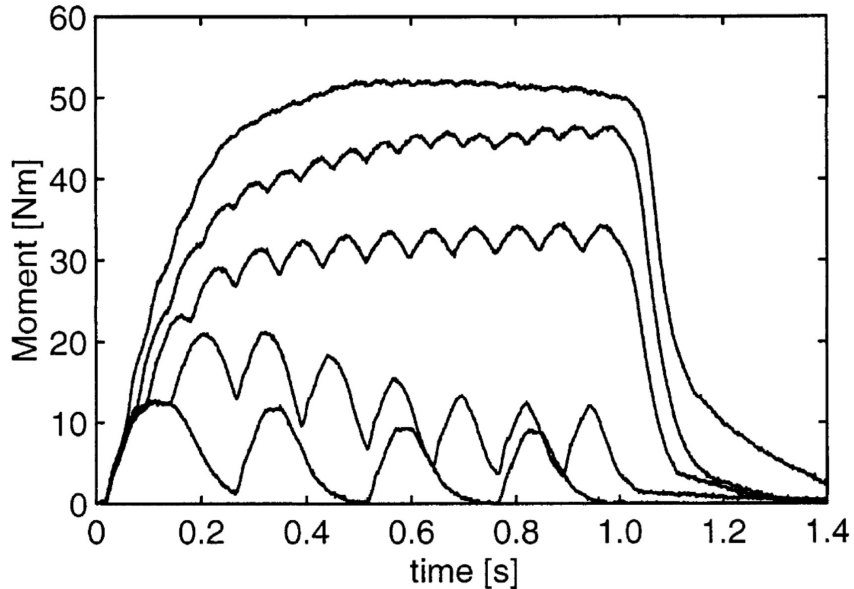


Figure 1-12: The summation of successive muscle twitches results in tetanic contraction, with increasing force shown by the moment generated by the muscle [25]

1.6.2 Task Planning and Motion Execution

Task and motion planning is hierarchical. A high level goal is formulated, stereotyped motion primitives are mapped to the movement, and then specific muscle activation patterns are triggered. Much work has gone into discovering the coordinate space and types of internal models used for motion planning.

Early work in this area found that hand tangential speed patterns varied less than joint angles, velocities, or accelerations for different motions of the arm [26]. These hand velocities are very smooth, showing a roughly symmetric peak. Flash and Hogan proposed that motion planning for the hand is an optimization procedure for maximal smoothness; that is, to minimize the mean-squared jerk. Smooth movements decrease higher order derivatives, which would allow planning further into the future in the face of uncertainty and noise. Describing the hand trajectory in task space Cartesian

coordinates, the minimum jerk condition is achieved by minimizing the functional

$$C(q(t)) = \frac{1}{t_f - t_0} \int_{t_0}^{t_f} \left(\frac{d^3 q}{dt^3} \right)^2 dt \quad (1.8)$$

where C is the mean-squared jerk, t_0 and t_f are the starting and ending times of the movement, and q is a vector of task space coordinates defining the trajectory. For point to points motions starting and ending at rest, this is solved by the per-coordinate trajectory

$$x(t) = x_0 + (x_f - x_0)(10\tau^3 - 15\tau^4 + 6\tau^5) \quad (1.9)$$

where x_0 and x_f are starting and ending positions and $\tau = \frac{t}{t_f}$ is the position along the trajectory. This solution can reproduce observed straight-line trajectories and symmetric bell-shaped speed profiles. This result is even stronger than it at first seems. The minimum jerk criterion in this form is also capable of describing the maximally smooth, continuously curved paths taken when moving between points through an intermediate waypoint [27].

Flanagan and Rao used visual distortion, transforming straight Cartesian hand paths to curved onscreen paths, to assess the domain of motion planning. After an adaptation period, subjects were able to execute straight line motion in the perception space, even though these were curved hand paths [28]. Together, these studies provide strong evidence that kinematic motion planning occurs in the task space, though this does not confirm how the brain conceptualizes the process.

However, kinematic models alone are not sufficient for the execution of motion plans. Definitionally, a kinematic model would be incapable of compensating for disturbances. Shadmehr and Mussa-Ivaldi applied mechanical perturbation in the form of a velocity dependent force-field during point to point reaching movements. At first, the resulting trajectories were curved, though the subjects could reach the final point after a time. With practice, the trajectories became approximately straight paths once again. When the force-field was turned off, the paths remained curved in the other direction until deadaptation was complete. This suggests that a feed-forward model was learned to compensate for the disturbance, but as the trajectories

following adaptation were straight, planning still must occur in the task space. Thus, the authors concluded that the dynamics of a motor task must be represented in the joint coordinate space [29].

Indeed, Bastian et al. tested dynamic movements of different speeds in subjects with cerebellar damage and found that their ability to coordinate torques at multiple joints was greatly diminished versus healthy controls. For slow movements, curved paths in Cartesian space were observed, while at high speed, there was overshoot in the motions. Further, the velocity profiles for subjects with cerebellar ataxia did not match those predicted for maximally smooth motion. The cerebellum must then be involved in coordinating joint torques via an internal model of the body; this is the so-called computed torque hypothesis [30]. With this evidence, it's clear that human motor control takes place through a combination of kinematic task space path planning and dynamic joint space motion execution.

1.6.3 Speed-Accuracy Tradeoff

Another strongly replicated result in the study of human motor control is Fitts' Law. Proposed by Paul Fitts in 1954, this model predicts that the time needed to complete a task increases with the task difficulty [31]. In his original paper, Fitts uses a reciprocal tapping task where targets of width W are separated by a distance $2D$. The index of difficulty (ID) of the task is calculated analogously to the signal to noise ratio,

$$ID = \log_2\left(\frac{2D}{W}\right) \quad (1.10)$$

Then, if this index is adjusted by the movement time (MT), the index of performance (IP) is

$$IP = \frac{ID}{MT} \quad (1.11)$$

A linear regression can be performed between the movement time and the index of difficulty to compare devices for completing a task. This takes the form

$$MT = a + b \cdot ID \quad (1.12)$$

where a and b are task-device specific constants. The lower the value of b , the less the movement time depends on the difficulty of the task; in most cases, a shorter movement time is desirable, so the slope of the regression line can be used to inform choices between devices. In fact, this was used to support Xerox's introduction of the computer mouse as an input device. Fitts' Law has been found to hold across a range of different media, including the movement of different limbs [32] [33], with input devices [34], and even underwater [35].

In 1956, an alternative formulation of Fitts' Law was proposed by Crossman that assesses task performance as executed rather than as requested. The ID for a movement is found using the effective width, which is

$$W_e = 4.133\sigma \quad (1.13)$$

where σ is the standard deviation of the actual points hit during the task [36]. Assuming the points reached are normally distributed, this range covers 96% of the distribution. Thus, the ID is adjusted for accuracy - lower performance, defined as greater standard deviation in points reached, lowers the ID. When MT also decreases, this formulation can better demonstrates the speed-accuracy tradeoff, which is how Fitts' Law is commonly used in the analysis of control schemes for prosthetic limbs [37] [38].

THIS PAGE INTENTIONALLY LEFT BLANK

Chapter 2

Methodology

This chapter describes techniques for creating a personalized and simplified model of the upper extremity that can be used for electromyographic control of a prosthetic arm. Such a model uses virtual muscle pairs modeled on the agonist-antagonist myoneural interface as the sole actuators for virtual joints that correspond to degrees of freedom to be controlled on a myoelectric prosthesis . The model translates user intent into approximate trajectories that are able to be used as reference signals for the low-level joint controllers found on powered upper extremity prostheses. The relevant physiological data needed to build the model, as well as the instruments needed to collect the data, are introduced. Then, the methods to process the data and to optimize the neuromuscular model are explained. A discussion of how the model's performance is validated follows. This methodology is applied to generate a model during a case study of a subject with unilateral upper extremity amputation.

2.1 Data Collection

2.1.1 Subjects

A single subject with unilateral elective upper extremity amputation was recruited for this study. Subject P1 (32 years old, 1.77 m, 77 kg) has a left transhumeral amputation and 2 AMI pairs. One pair is constructed from the long bicep (LB) and

long tricep (LT) to primarily control the elbow joint. The other is a regenerative construct; the short biceps (SB) was reinnervated with the median nerve to control flexor muscles of the hand and the short triceps (ST) was reinnervated with the radial nerve to control extensor muscles of the hand, following the techniques developed in [39]. For clarity, these muscles will be referred to by their native function. The nerves were transected at a high enough level such that the subject trying to move multiple different joints in the hand causes depolarization of the muscles. Therefore, this AMI pair cannot be assigned to a singular degree of freedom. Subjects P1 is right hand dominant with normal vision. Experiments were conducted after obtaining informed consent from the subject under a protocol approved by the Massachusetts Institute of Technology (MIT) Committee on the Use of Humans as Experimental Subjects.

2.1.2 Electromyography

All electromyographic (EMG) signals were collected using an Arduino-based header board developed in the Biomechatronics Group at the Massachusetts Institute of Technology Media Lab. The board can support up to 16 channels of bipolar EMG, streaming wirelessly for offboard processing in real time at 2000 Hz.

Surface EMG

Adhesive wet surface electrodes were used to record the EMG data. The skin's surface was cleaned with isopropyl alcohol wipes before two redundant pairs of gel electrodes were placed near the muscle bellies for each AMI construct. That is, two pairs were placed on each of the short biceps, short triceps, long biceps, and long triceps for a total of 8 channels of bipolar EMG. Table 2.1 indicates where each of the channels was placed. Each electrode was connected to the board via 1.5 m shielded cable. The residual limb was wrapped in an elastic bandage to hold the electrodes in place and to isolate the muscle signals from motion artifacts.

Table 2.1: Location of the 8 channels of bipolar EMG on P1's residuum

Muscle	Channels	
Long triceps	Ch0	Ch1
Long biceps	Ch2	Ch3
Short triceps	Ch4	Ch5
Short biceps	Ch6	Ch7

EMG Processing

The raw EMG signal was streamed wirelessly at 2000 Hz to a computer for real time processing via Python script. A fourth order 3 Hz high-pass infinite impulse response (IIR) Butterworth filter was applied to each channel to remove motion artifacts and drift. Then, 3 fourth order bandstop IIR Butterworth filters (58 - 62 Hz, 118 - 122 Hz, 178 - 182 Hz, respectively) were applied successively to insulate the recording from 60 Hz alternating current electrical noise. At this point, the noise level, in mV, of the filtered signals were noted to be used for normalization. The filtered data was rectified and normalized by subtracting the noise levels observed and then dividing each channel by the highest EMG amplitude observed during maximum voluntary contraction (MVC). The normalized EMG was low-pass filtered at 8 Hz with a fourth order IIR Butterworth filter to approximate integrated EMG (iEMG) with a 125 ms recording window. The iEMG was then downsampled to 60 Hz for simulation. See Buchanan et al. to support this processing pipeline [40]. The processed iEMG was used as a proxy to muscle activation as input for the neuromuscular model.

2.1.3 Single Degree of Freedom Kinematic Tasks

The subject was asked to imagine moving each degree of freedom that will be included in the model smoothly, cyclically, and in isolation to generate kinematic data. For 30 seconds each, the subject moved their phantom joints through their full ranges of motion, taking care to move continuously. EMG was simultaneously recorded from their AMI constructs and processed as detailed above. The subject was instructed to move naturally, exerting no more than half his maximal voluntary effort. The motions were completed at a self-selected and varied pace. This ensured that multiple muscle

activation patterns were collected so that the model would not be overfit to movement at a specific frequency.

2.1.4 Kinematic Profile Reconstruction

The trajectories the subject executed were recreated by leveraging the minimum jerk observation. Though maximally smooth trajectories are observed in hand point-to-point movements, by instructing the subject to move their joints smoothly through their full ranges of motion, smooth kinematic profiles were assumed. When the activation levels of antagonist muscles cross, with one increasing and the other decreasing, during the kinematic oscillation tasks, it was assumed that the joint was in its neutral position. As the AMI recipient does not have to actuate any configuration dependent inertia, the crossing of the activation levels indicated the crossing of the neutral position rather than the deceleration of the limb in preparation for a change in direction. By finding the times when these activations were equal with a Python script, the zero crossings for each joint were extracted. These zero crossing timings were verified by hand to ensure no points were missed.

The timings and the joints' maximum angles were input into a Python script that used optimization to recreate a maximally smooth trajectory. The objective function for this optimization was the mean-squared jerk over the course of the trajectory, as in equation 1.8. A candidate trajectory was generated by fitting four fifth-order polynomials between consecutive zero crossings such that the position and its first two time derivatives were continuous at the crossings. Between the zero crossings, the first segment was from the neutral position to the maximum of the joint's range of motion in one direction, the second returned to neutral, and the final two segments corresponded to the same movement in the other direction. Six boundary conditions are required for each polynomial; the neutral position, the joint's maximum range of motion, zero velocity, and zero acceleration provided four of the necessary boundary conditions. The other two - a second velocity and a second acceleration - and the timing of the peak between zero crossings were decision variables in the optimizer. The optimizer used Sequential Least Squares Programming and up to 50,000 iterations to

find the trajectory that minimized the mean-squared jerk over the trajectory. The resulting trajectories oscillated smoothly between the joint's minimum and maximum joint angles. With these reference trajectories and the processed EMG, the muscle and joint parameters for the complete neuromuscular model were found.

2.2 Neuromuscular Model Generation

2.2.1 Model Design

A simplified neuromuscular model for four degrees of freedom in the arm was created for this work. The modeled degrees of freedom are flexion and extension of the elbow (referred to as elbow), opposition of the thumb (thumb), flexion and extension of the index finger (index), and flexion and extension of the 3rd through 5th digits (digits). These degrees of freedom correspond to those for which the subject has AMI constructs.

The full virtual muscle model of the arm was designed with two principles in mind:

- All models are wrong, but some are useful - models should be as simple as possible to capture the desired phenomena, but no simpler,
- Model parameters should fall in near-biological ranges to maintain the connection between model and physical muscles.

Noting these requirements, the simplest model that can replicate the dynamics of the biological limb would consider a single agonist-antagonist pair actuating a single rigid body with fixed inertia about the joint axis for each degree of freedom. The muscles are treated as Gasser-Hill muscle tendon units, as presented by Shadmehr and Arbib in [16], with parameters found through an optimization procedure and forward dynamics simulation.

A representative model for a single degree of freedom is shown in Figure 2-1.

This model shows two MTUs with fixed origins inserting at a distance L2 along the rigid body segment. The distance L3 is the distance of the origin of the virtual

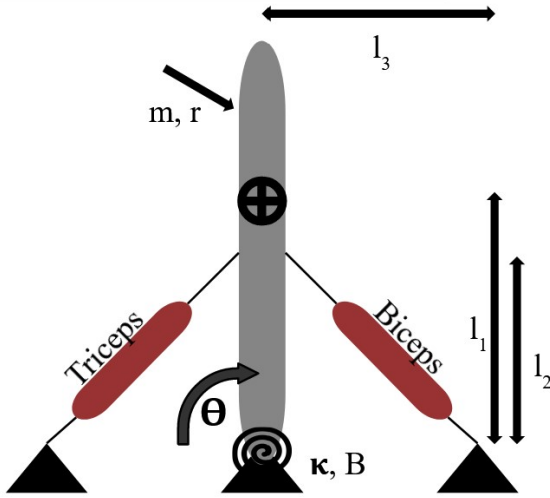


Figure 2-1: 2D model of virtual agonist-antagonist pair actuating single degree of freedom. Figure not drawn to scale.

muscle from the joint axis of rotation. These distances and the joint angle can define the length of the MTU. Each single virtual muscle replicates the action of multiple native muscles, so the MTU length can vary over a larger range than in the biological limb such that the forces generated are approximately equal to those of the multiple muscles. The length of the MTU and the joint angle are used to calculate moment arm of the muscle according to equation 1.5. The torque generated by each muscle is calculated with the moment arm and the force in the MTU, as in equation 1.3. The joint has a lumped parameter κ representing stiffness and a lumped parameter B representing damping. Stiffness arises from the elasticity of passive ligaments around the joint while damping accounts for the energy loss from sliding tissues and heat generated by the muscles. The limb segment actuated by the virtual muscle pair is modeled as a single rigid body with mass m , with the distance to its center of mass L_1 , and radius r . The inertia of the limb segment is calculated as that of a massive cylinder with uniform density rotating about its end, corresponding to the mode of movement for the modeled joints. The digits were treated as a single rigid body with the mass of three fingers. These physiological parameters were fixed for each joint, modified from average body segment parameters as reported in [41]. The fixed origin and insertion lengths are identical for the muscles comprising each virtual joint. Table

2.2 summarizes the fixed parameters used to generate the model.

Table 2.2: Fixed Physiological Parameters for four Degree of Freedom Model

Joint	L1	L2	L3	r	m	J
Elbow	0.301 m	0.099 m	0.500 m	0.030 m	1.64 kg	0.050 kg·m ²
Digits	0.090 m	0.030 m	0.149 m	0.009 m	0.082 kg	2.23e-4 kg·m ²
Thumb	0.054 m	0.018 m	0.090 m	0.014 m	0.123 kg	1.25e-4 kg·m ²
Index	0.090 m	0.030 m	0.149 m	0.009 m	0.246 kg	6.69e-4 kg·m ²

2.2.2 Optimization Formulation

Muscles are highly nonlinear systems whose outputs in simulation are very sensitive to initial conditions and parameter values. Thus, it is best to use a global optimization solver rather than a gradient based method. In this work, MATLAB's genetic algorithm (GA) toolbox was used to find optimal muscle parameters. For each possible parameter set, virtual muscles were defined with the given physiological parameters. These virtual muscles were arranged in agonist-antagonist pairs at each virtual joint, as described in section 2.2.1. The time synchronized iEMG, processed as in section 2.1.2, and reference trajectories, generated as written in section 2.1.4, were passed as inputs to the optimizer. All data used to generate the optimized model is shown in Figure 2-2. As is seen in the figure, there is a high degree of coactivation between the two pairs of muscles in the subject's residual limb; without studying muscle activation patterns during other movements, all that can be said is that this coactivation modulates joint stiffness.

Each generation contained 20,000 members, with 20 elite members surviving between generations. Optimization terminated after 50 generations. This resulted in roughly 1 million evaluations of the cost function, allowing a thorough search of the parameter space. The cost function and constraints were vectorized to take advantage of vectorized processing in MATLAB; a complete GA run could be completed in about 1 hour on an Intel i9-12000K CPU.

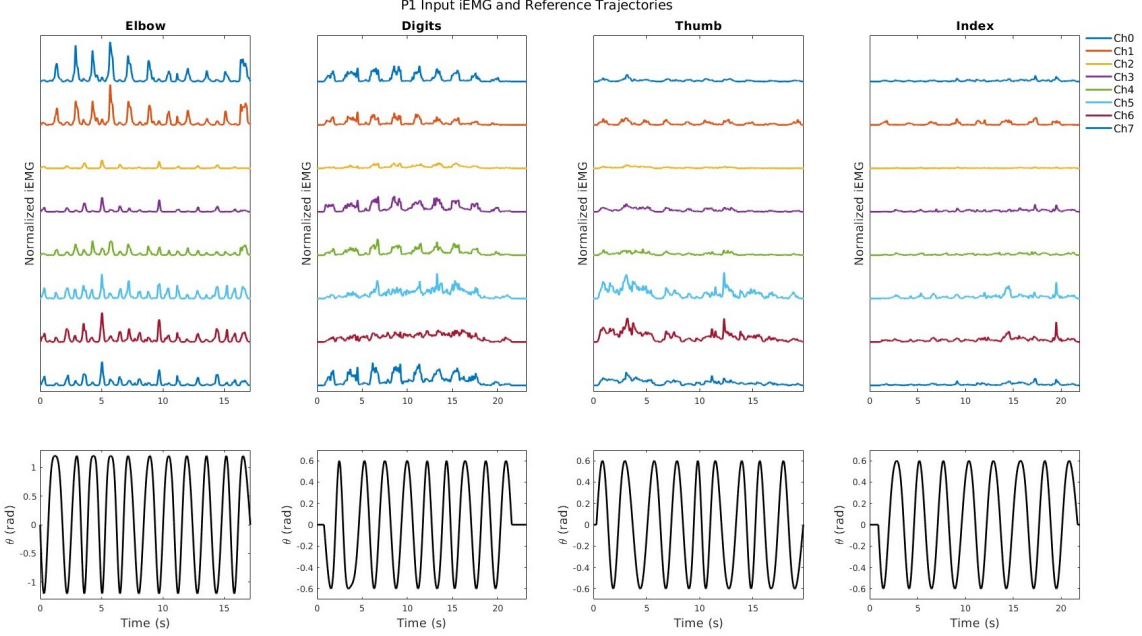


Figure 2-2: Processed iEMG and smooth reference trajectories for the four joints used as input data.

Optimization Parameters

The Shadmehr-Arbib muscle model uses five parameters to characterize the behavior of an areflexive muscle. These are:

- f_{max} , the maximum isometric force the muscle can produce,
- l_{opt} , the length at which the muscle's active force-length curve peaks,
- K_{SE} , the series elastic spring constant, representing the stiffness of the tendon,
- K_{PE} , the parallel elastic spring constant, capturing the passive force-length behavior of the muscle,
- b , is the resistance to force generation during muscle shortening, defining the force-velocity relationship.

For each degree of freedom, a rotational stiffness constant, κ , and a rotational damping constant, B , were included as well. For 8 muscles and 4 virtual joints, there were 48 total physiological optimization parameters.

In addition to these muscle parameters, the optimizer also searched for an iEMG weighting matrix. This stands in for a synergy matrix, acting as a pattern recognition layer. As mentioned above, there is a high degree of coactivation seen between channels of iEMG, so the inclusion of this matrix allowed a relatively small number of control inputs to generate control signals for a broader range of virtual joints by distinguishing between muscle activation patterns. With 8 channels of EMG recorded and 8 virtual muscles, there were 64 additional decision variables.

Constraints

Each physiological parameter was bounded to stay within approximately human ranges. Estimates for upper extremity muscle stiffness were found in [42]. Tendon stiffness bounds were based on [43]. Using maximum moment values from [44] and moment arms from [45], the maximum isometric force of each muscle were estimated. The bounds were chosen such that these estimates fall towards the middle of the range of possible values. This makes the ranges wider than is found within the biological limb; as mentioned above, the virtual muscles had to be capable of producing forces equivalent to the multiple muscles they represented. The optimal length bounds were stricter - the MTU length is fundamentally limited by the joint geometry. The bounds were then the length of the MTU when the joint is fully flexed and the length of the MTU when the joint is fully extended (because the muscle attachments are symmetric about the joint, the same upper and lower bounds applied to both the flexor and the extensor). Table 2.3 shows the bounds on the physiological parameters.

The iEMG weights also had simple bound constraints. Each channel was constrained between -1 and 1 for each muscle. Then, a positive weight would indicate that a muscle should more often contract when the iEMG on that channel is high. A negative weight would show that the antagonist muscle more often contracts when iEMG on that channel is high.

Table 2.3: Bounds on Physiological Decision Variables

Parameter	Elbow	Digits
f_{max} (N)	$40 \leq f_{max} \leq 4000$	$3 \leq f_{max} \leq 300$
l_{opt} (m)	$0.400 \leq l_{opt} \leq 0.599$	$0.120 \leq l_{opt} \leq 0.179$
K_{SE} (N/m)	$50 \leq K_{se} \leq 2000$	$50 \leq K_{se} \leq 2000$
K_{PE} (N/m)	$50 \leq K_{pe} \leq 2000$	$50 \leq K_{pe} \leq 2000$
b (N · m · s)	$5 \leq b \leq 300$	$5 \leq b \leq 300$
κ (N · m/rad)	$0 \leq \kappa \leq 20$	$0 \leq \kappa \leq 20$
B (N · m · s/rad)	$0 \leq B \leq 3$	$0 \leq B \leq 3$

Parameter	Thumb	Index
f_{max} (N)	$40 \leq f_{max} \leq 4000$	$3 \leq f_{max} \leq 300$
l_{opt} (m)	$0.072 \leq l_{opt} \leq 0.107$	$0.120 \leq l_{opt} \leq 0.179$
K_{se} (N/m)	$50 \leq K_{se} \leq 2000$	$50 \leq K_{se} \leq 2000$
K_{pe} (N/m)	$50 \leq K_{pe} \leq 2000$	$50 \leq K_{pe} \leq 2000$
b (N · m · s)	$5 \leq b \leq 300$	$5 \leq b \leq 300$
κ (N · m/rad)	$0 \leq \kappa \leq 20$	$0 \leq \kappa \leq 20$
B (N · m · s/rad)	$0 \leq B \leq 3$	$0 \leq B \leq 3$

Cost Function

The optimization used a cost function based on the results of a forward dynamic simulation. First, the model muscles were defined with the parameters from a candidate set. The Shadmehr-Arbib model defines a differential equation for the rate of change of force generated by the model muscle based on the current MTU length and the muscle activation. The muscle activation was found by multiplying the synergy weights by the iEMG at that time step. This yielded one net muscle activation per muscle in the model for each time. The current MTU lengths were calculated from the geometries of the joints and their fixed attachment points. The rate of change in velocities of the joints was calculated using equation 1.6. The rate of change in position of a joint was simply its velocity. These four state equations for each joint were numerically integrated with a 4th-order fixed timestep Runge-Kutta scheme to calculate the full joint trajectories. The time step was 0.0167 seconds, corresponding to the EMG sampling rate.

The cost for a given parameter set was then found with the single objective cost

function

$$C(\Theta(t), \Theta_{ref}(t)) = \sum_{j=1}^4 \sum_{t=0}^{n-1} (\theta_j(t) - \theta_{j,ref}(t))^2 \quad (2.1)$$

where Θ and Θ_{ref} are the model trajectories and input trajectories for all four joints, respectively, j is the index counting over the four joints of the model, and t is the discretized time index. This cost is the sum over the four joints of the residual sum of squares between each reference and candidate joint trajectory.

2.3 Model Validation

The optimized dynamic model was used to generate trajectories with iEMG collected during various motor tasks. This allows analysis of the results of the optimization procedure and assessment of the model's ability to replicate natural human biomechanics. This can support the use of such a biophysical model within the control system for a robotic upper extremity prosthesis.

2.3.1 Trajectory Analysis

Immediately after optimization, the estimated muscle activations from the single degree of freedom kinematic tasks were fed through the model to find the corresponding joint trajectories. For both the input and output kinematics, the dimensionless log jerk (DLJ) was calculated to quantify the smoothness of the movement. Used with the coefficient of determination, these represent the 'best performance' of the model - it is expected that these trajectories would match most closely with the input.

2.3.2 Muscle Dynamics

Each muscle was excited independently with an impulse equivalent to 10% of its maximum force. An impulse of this magnitude represents force approximately equivalent to the twitch following one action potential. As this model is a mass-spring-damper system, the response of the joint to this single excitation can show whether the optimized muscles behave like true muscles. This test also showed how symmetric the

muscles in the optimized model are about their joint.

2.3.3 Fitts' Law

In addition to the maximally smooth motion kinematic tasks, the subject also performed a series of oscillations starting from rest in the neutral position at specified frequencies while EMG was recorded. He was tasked with moving through each joint's full range of motion in time to a metronome at 15 beats per minute (BPM), 20 BPM, and 25 BPM. This EMG was processed as above, with the estimated iEMG used to calculate optimized model trajectories. For each model trajectory, the dominant movement frequency was found from the power spectral density (PSD) of the output. The PSD was approximated using Welch's method, which was chosen as it can reduce the estimate's noise. The trajectories were first detrended by the subtraction of a best-fit line. The number of Fast Fourier Transform points used was the largest power of 2 less than the length of the input time vectors. If this number was nFFT, Gaussian windows of length nFFT with overlap of nFFT/2 were used in the estimate. The frequency with the highest power from the PSD was considered the dominant movement frequency and quantified whether the model's output oscillations matched their targeted frequencies.

Based on Fitts' Law, it was expected that the index of performance would decrease as the movement frequency increased. Equivalently, using the effective width form, the standard deviation of the peak distance reached in each cycle would increase with movement frequency. The standard deviation was calculated with the peak positive distance from neutral for 10 consecutive cycles at each movement frequency. The mean of these peak-to-peak times was taken as the movement time. The end of a joint's range of motion is the target position, D . With these values, the indices of difficulty and performance were calculated. A linear regression over the movement times and indices of difficulty was performed and the best-fit lines were plotted for each joint. A positive slope for these lines indicated that the model's output behavior matched the predictions of Fitts' Law.

2.3.4 Graded Control

The model was also tested on non-periodic movements. Movements of the arm are not often cyclical, so any competent model should move point-to-point as well. To this end, the subject completed a series of random position tasks as EMG was recorded. The subject was asked to move to one of 5 positions evenly spaced through each joint's range of motion as directed by an onscreen prompt. For example, the subject moved the elbow between full extension, half extension, neutral, half flexion, and full flexion. Each position was displayed onscreen for 1.5 seconds, with a 1.5 second rest period between to return to neutral. The order of presentation was randomized and 10 repetitions were completed for each position. The collected EMG was used to simulate the executed trajectories. These trajectories were used to determine the ability of the model to reproduce movement to distinct positions. The complete trajectory was split into chunks by target position and the mean position of the joint for each repetition at each position was calculated. For each joint, a multiple comparisons test with the Bonferroni correction at significance level $\alpha = 0.1$ was used to determine the model's ability to produce distinct levels of movement at intervals smaller than the full joint range of motion. This significance level was chosen due to the small number of samples at each target position.

THIS PAGE INTENTIONALLY LEFT BLANK

Chapter 3

Results

This chapter presents the arm model and the results of analysis performed to assess its ability to replicate natural biomechanics. The parameters of individual muscles and their impulse responses can demonstrate their similarity to biological muscles. Then, regression on movement at different speeds shows whether model virtual joints behave as predicted by Fitts' Law. Lastly, the model's ability to generate outputs proportional to input intensity is considered.

3.1 Optimized Neuromuscular Model

3.1.1 Optimal Parameter Set

The optimal muscle parameter set found for the 4 degree of freedom arm model is shown in Table 3.1. Parameters are separated by the corresponding virtual joint and then by individual muscle. The optimal EMG weighting matrix can be seen in Table 3.2. Figure 3-1 shows the kinematic trajectories generated by the resulting model overlaid with their reference trajectories from Figure 2-2. The dimensionless log jerk of the reference trajectories and model generated trajectories are contained in Table 3.3. Unless otherwise indicated, positions are given as deviations from the center of the joint range of motion in all figures and tables.

Table 3.1: Optimized Muscle Parameters

Parameter	Elbow		Digits		Thumb		Index	
	Biceps	Triceps	FDS	ECU	AIN	EPL	FDP	EIP
f_{max}	3971 N	3926 N	296.7 N	297.7 N	199.8 N	196.6 N	99.74 N	98.07 N
l_{opt}	0.593 m	0.579 m	0.179 m	0.176 m	0.107 m	0.100 m	0.163 m	0.178 m
K_{SE}	1865 N/m	1954 N/m	1987 N/m	1998 N/m	1915 N/m	1785 N/m	1135 N/m	1035 N/m
K_{PE}	128 N/m	545 N/m	58.97 N/m	129.2 N/m	50.22 N/m	201.3 N/m	197.5 N/m	270.7 N/m
b	11.87 N·s/m	15.14 N·s/m	12.22 N·s/m	48.08 N·s/m	17.59 N·s/m	33.67 N·s/m	8.222 N·s/m	7.635 N·s/m
κ	19.97 N·m/rad		0.706 N·m/rad		0.115 N·m/rad		0.128 N·m/rad	
B	0.670 N·m·s/rad		0.015 N·m·s/rad		0.007 N·m·s/rad		0.0003 N·m·s/rad	

Table 3.2: Optimized EMG Weighting Matrix

Muscle	Channel 0	Channel 1	Channel 2	Channel 3	Channel 4	Channel 5	Channel 6	Channel 7
Biceps	0.8609	-0.09720	-0.9403	-0.9621	-0.9519	-0.0024	0.3805	-0.9290
Triceps	-0.9934	-0.5088	0.9623	0.9483	0.8971	0.4178	-0.2762	0.4648
FDS	-0.9778	-0.7446	-0.2824	-0.9624	-0.9193	0.6778	0.9082	-0.5650
ECU	-0.3116	-0.9456	-0.9297	-0.1362	0.1625	0.1825	-0.9781	0.6011
AIN	0.3313	-0.9957	-0.9789	-0.9535	-0.9686	-0.8356	0.9246	-0.1953
EPL	-0.4266	0.3873	0.8445	-0.9431	-0.4402	0.7631	-0.9878	-0.8749
FDP	-0.8992	-0.9496	0.9917	0.7361	0.9138	0.1412	0.8447	0.1498
EIP	0.9642	0.9820	-0.9882	-0.5924	-0.9176	0.3787	0.2244	0.1888

Table 3.3: Dimensionless Log Jerk from Reference and Optimized Trajectories

Joint	Reference	Model
Elbow	27.957	32.082
Digits	32.292	33.625
Thumb	30.527	32.915
Index	32.706	32.865

3.1.2 Model Muscle Impulse Responses

The joint position response to an impulse equal to 10% of each muscle's maximum force are shown in Figure 3-2. The responses for the two virtual muscles at each joint are overlaid, but were calculated independently. The peak amplitudes and peak times are shown in Table 3.4.

Table 3.4: Impulse Response Peak Amplitudes and Times

Muscle	Peak Amplitude	Peak Time
Biceps	0.134 rad	0.067 sec
Triceps	-0.134 rad	0.068 sec
FDS	0.113 rad	0.033 sec
ECU	-0.324 rad	0.045 sec
AIN	0.164 rad	0.027 sec
EPL	-0.257 rad	0.033 sec
FDP	0.128 rad	0.042 sec
EIP	-0.120 rad	0.042 sec

3.2 Demonstration of Natural Biomechanics

3.2.1 Fitts' Law Testing

Model-generated outputs using EMG collected during the single DoF fixed frequency oscillation tasks are shown in Figures 3-3 to 3-6. Also included are estimates for the power density spectrum of each signal, used to identify the dominant frequency of movement, which is included above the spectrum. The indices of difficulty (ID) and indices of performance (IP) are summarized in Table 3.5. Figure 3-7 shows the

P1 Reference and Optimized Trajectories

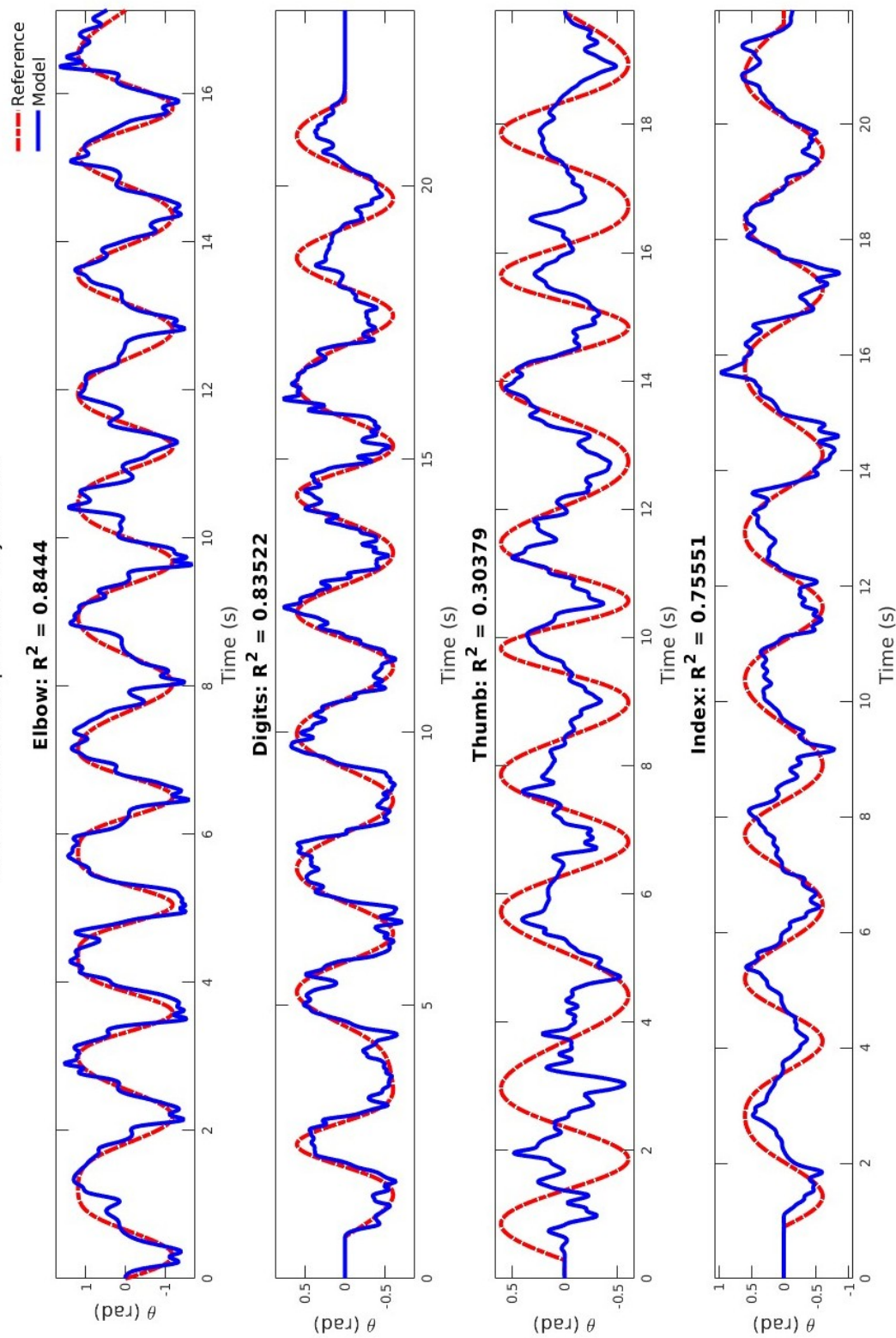


Figure 3-1: Trajectories generated by optimized model for the same EMG input that produced the trajectories. Coefficients of determination for each joint are shown.

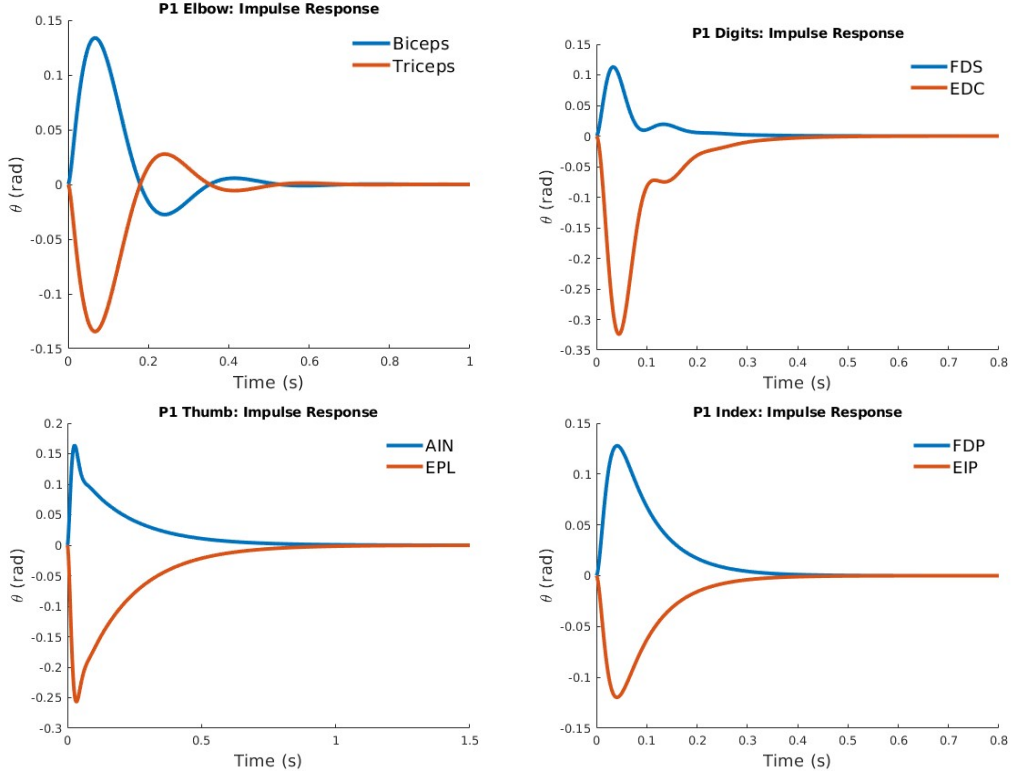


Figure 3-2: Responses of each joint to independently applied single muscle impulse

best-fit lines that define the linear relationship between ID and MT along with the explicit parameters a and b .

Table 3.5: Indices of Performance from Fitts' Law Testing

Joint	15 BPM		20 BPM		25 BPM	
	ID	IP	ID	IP	ID	IP
Elbow	5.46	1.51	2.73	1.05	2.11	1.10
Digits	4.89	2.60	3.30	2.30	2.89	2.30
Thumb	1.63	1.10	1.97	1.05	1.65	1.18
Index	1.51	0.50	1.69	1.09	2.23	1.77

3.2.2 Graded Control Tasks

Model Trajectories

A section of the trajectories generated from the optimized model for each joint during the graded control tasks are shown in Figure 3-8. These figures show the first 60 seconds of the full 120 second trials, which can be seen in Appendix A.

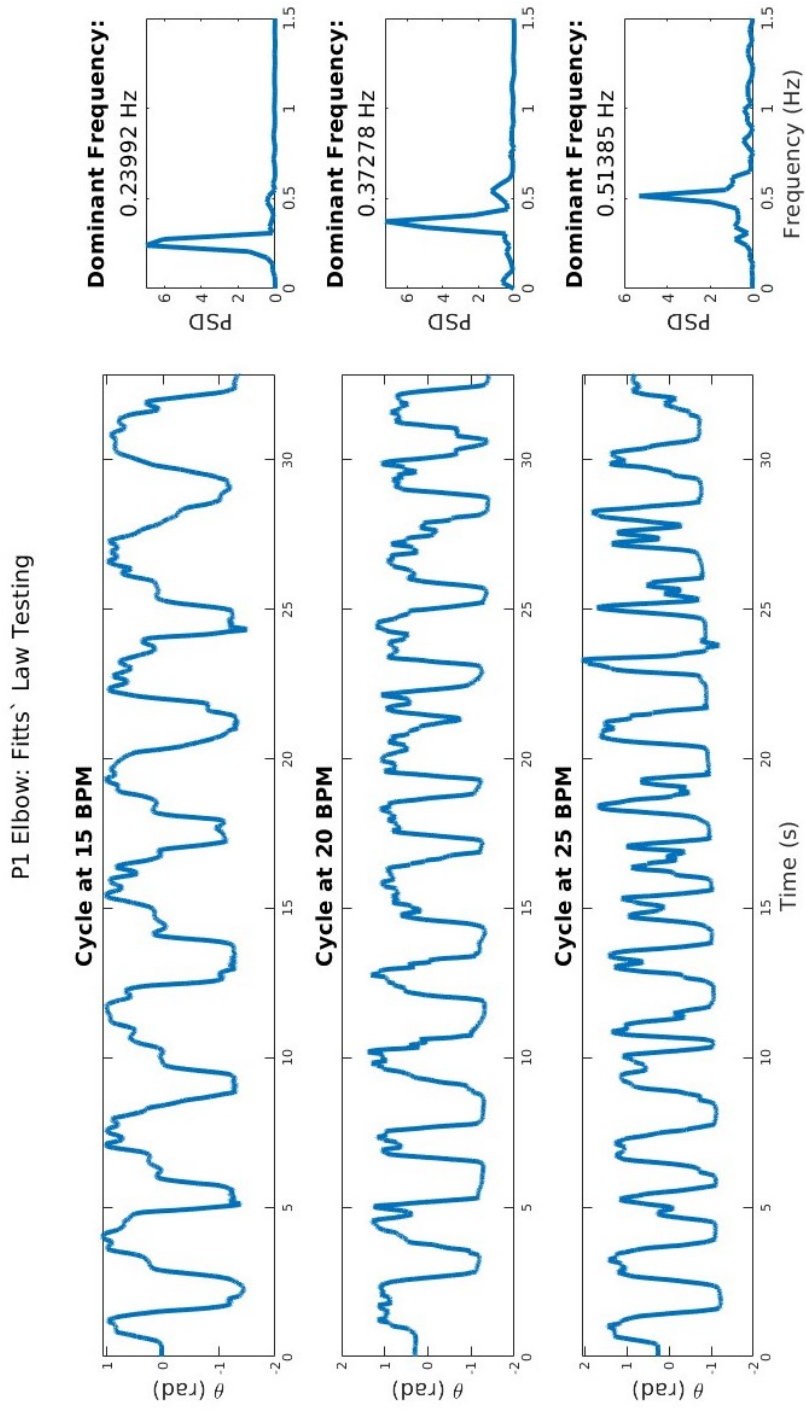


Figure 3-3: Model elbow joint trajectories using EMG collected during varied frequency testing. The dominant frequency for each trial is shown at right.

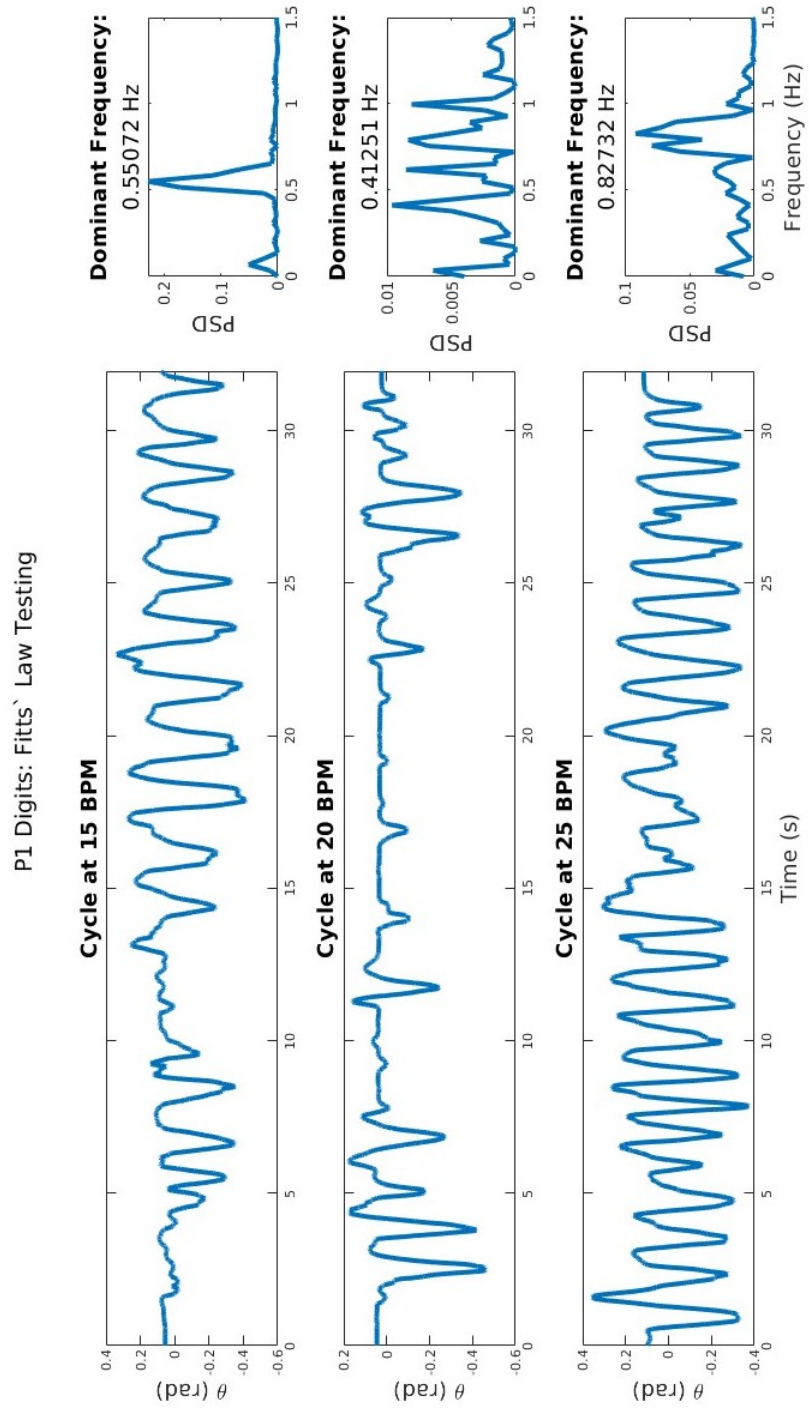


Figure 3-4: Model 3rd-5th digits trajectories using EMG collected during varied frequency testing. The dominant frequency for each trial is shown at right.

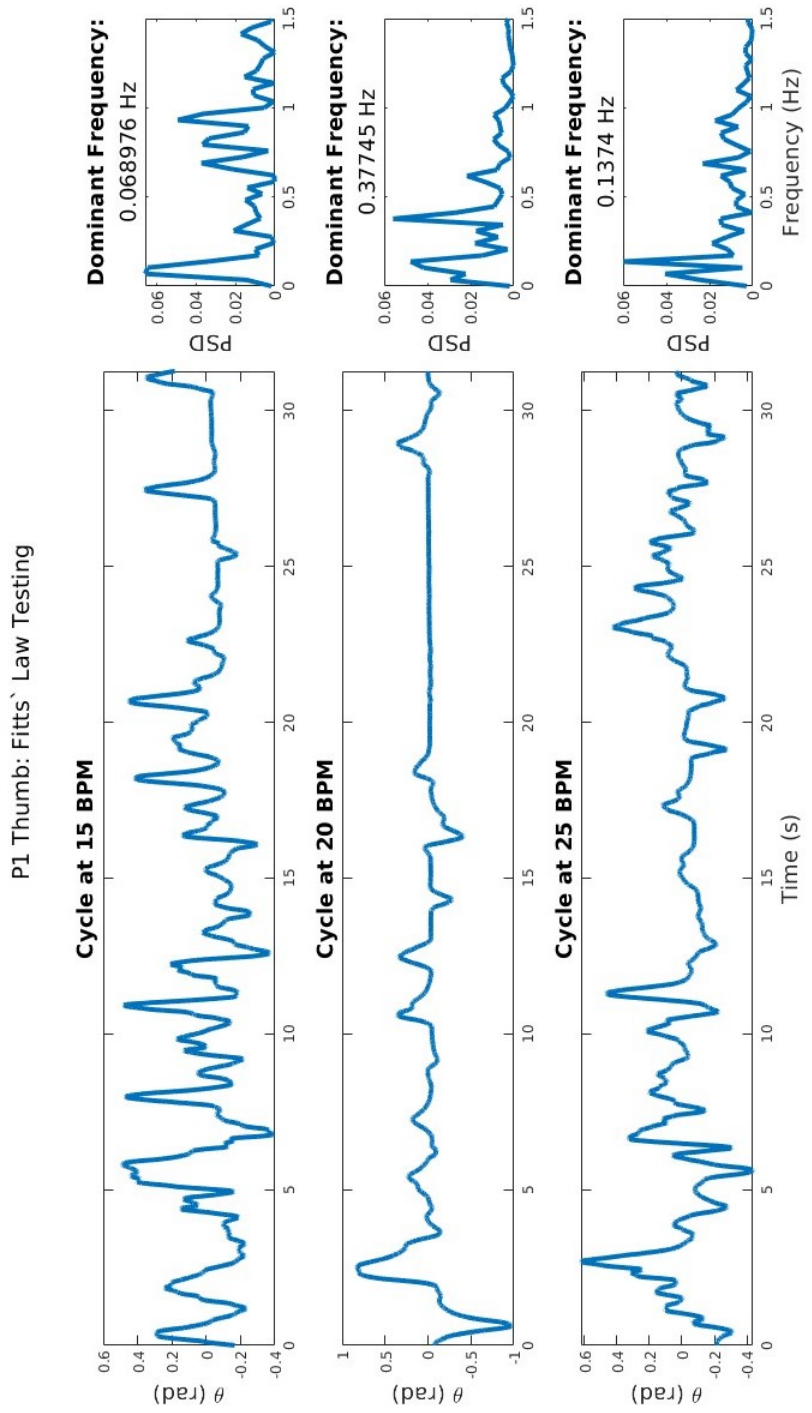


Figure 3-5: Model thumb trajectories using EMG collected during varied frequency testing. The dominant frequency for each trial is shown at right.

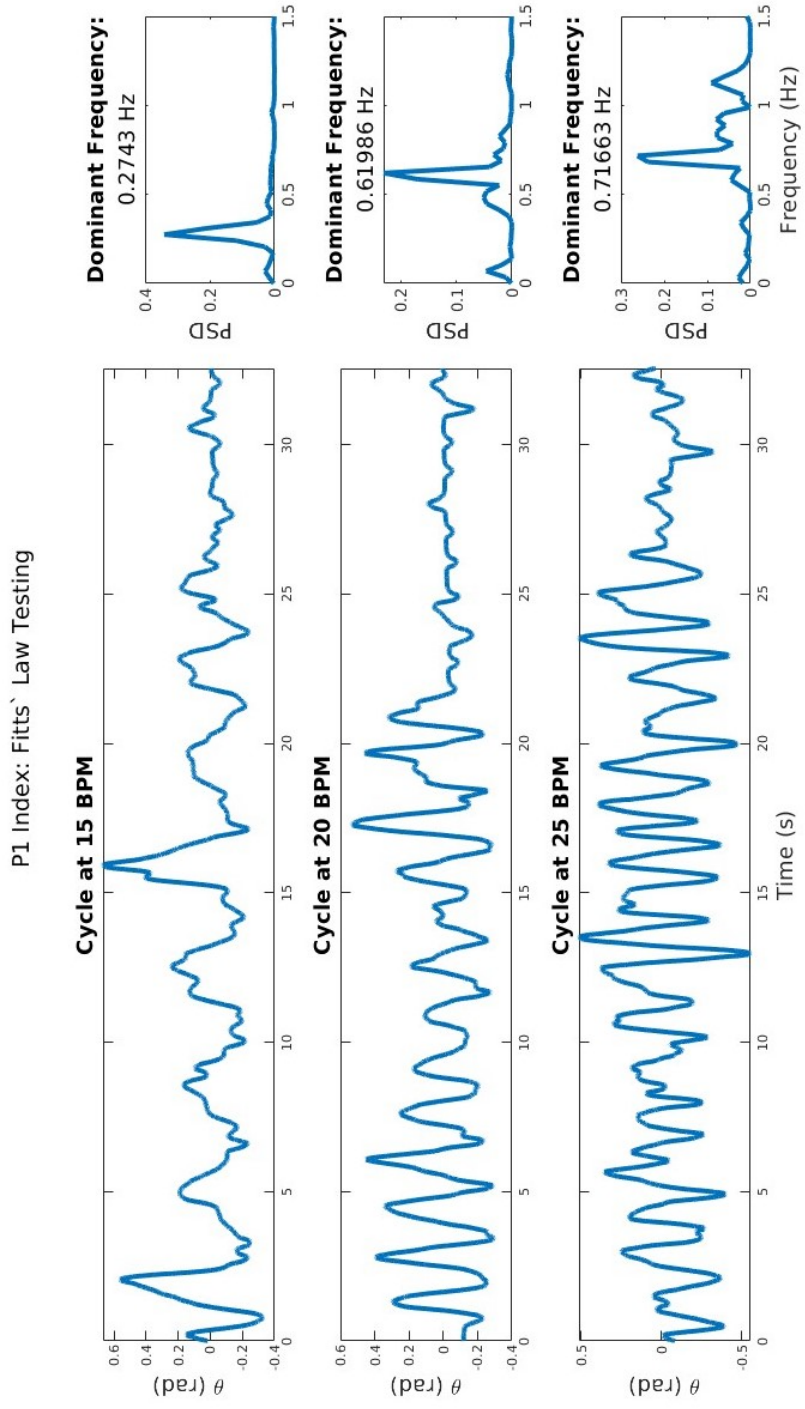


Figure 3-6: Model index finger trajectories using EMG collected during varied frequency testing. The dominant frequency for each trial is shown at right.

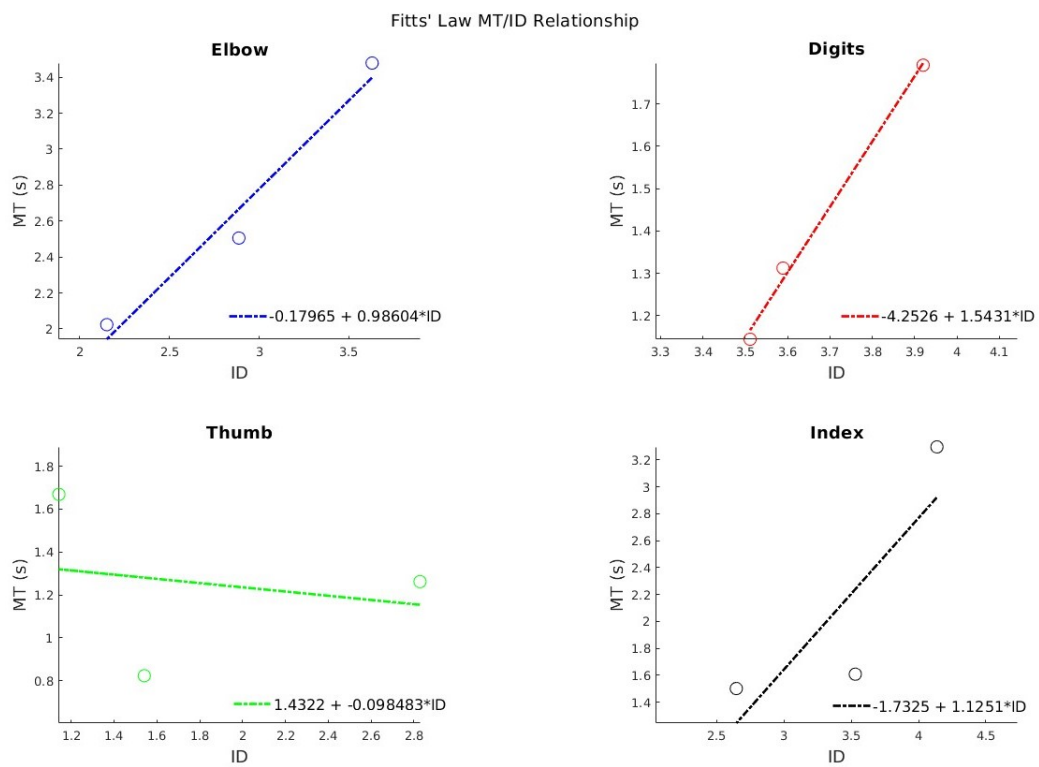


Figure 3-7: Linear relationships between ID and MT for motion of different speeds. The constants a and b that determine the equation of the line of best-fit are shown

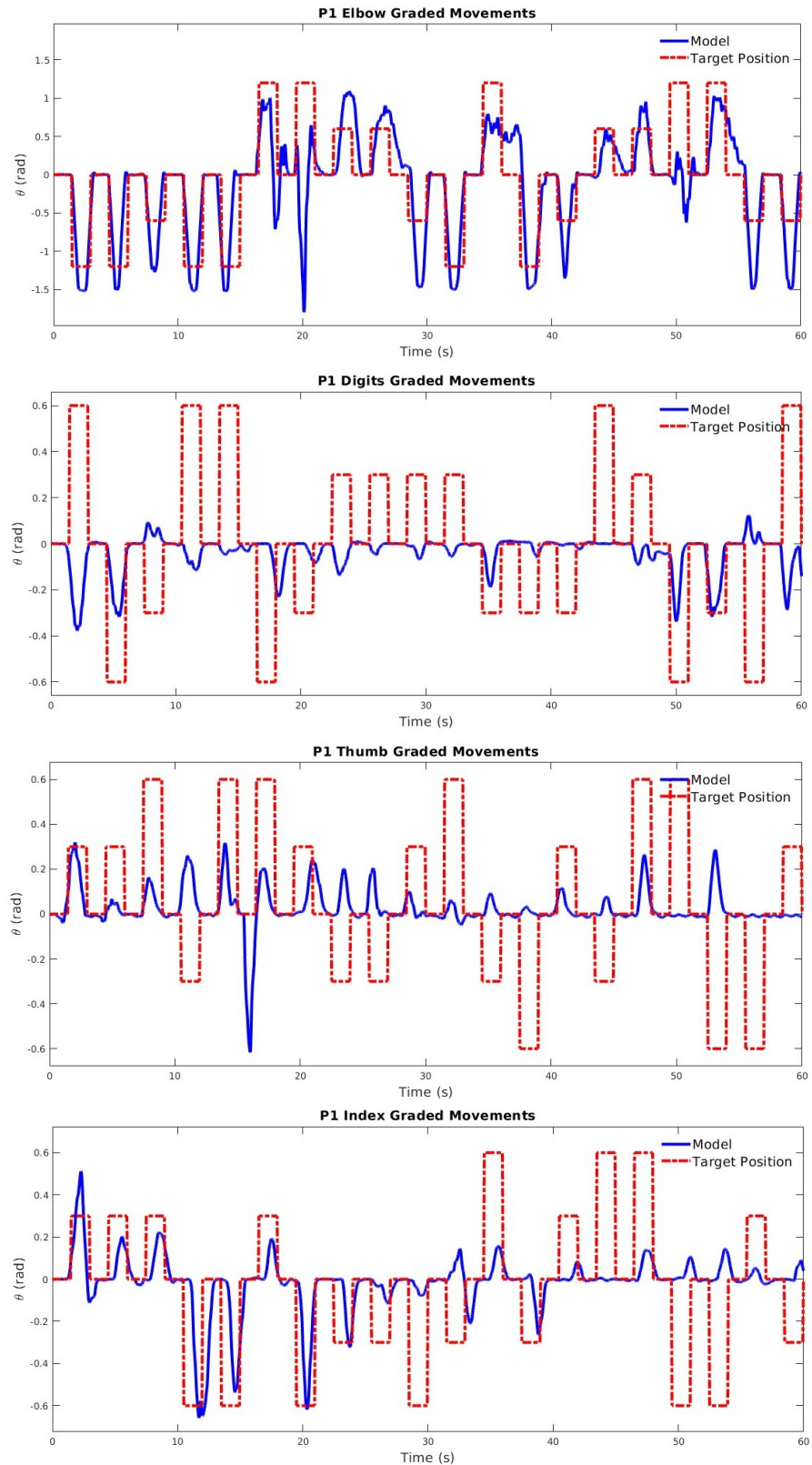


Figure 3-8: Model joint trajectories generated EMG collected during graded control tasks overlaid on the randomly presented target positions presented during each trial

Position Discrimination

Following these trajectories, in Figure 3-9, are bar charts showing the mean position of the virtual joints over the time periods the target position was in each of the five tranches. Error bars represent one standard deviation from the mean position in a given tranche. An asterisk above a bar indicates that the bar is statistically different from all other bars in the chart at significance level $\alpha = 0.1$. The p -values for pairwise likelihood of differences between the bars for each model joint are found in Table 3.6. Within the table, tranches are five equally spaced positions from the lowest target position to the highest target position in ascending order (-1.2 to 1.2 rad for the elbow, -0.6 to 0.6 rad for all other joints). Statistically significant pairwise differences from a multiple comparisons test following a Bonferroni correction are marked with an asterisk. Finally, Figure 3-10 summarizes the proportion of the time the mean direction of the model output matched the direction, from neutral, of the target position. These figures allow analysis of model performance for replicating subject intent without consideration of the magnitude of the output.

3.3 Subject's Comments

The subject reported on his perception of his control over his constructs during the motor tasks. He had the strongest active control over the AMI constructed for his elbow joint; these muscles are natively innervated, so this result is not surprising. He stated that he felt he could move his index finger separately from the rest of his digits, which otherwise felt like they were held together in a splint and moved together. The thumb provided the weakest sensation for the subject - the sporadic activation patterns with no clear peaks and troughs corresponding to activation of distinct antagonist muscles support his assertion.

Subject P1 found the oscillation tasks easier than the graded control tasks. These required him to focus only on moving each joint continuously rather than trying to stop in specific positions. In addition, the presentation of target positions for 1.5 seconds during the graded control tasks was as fast as he could keep up with.

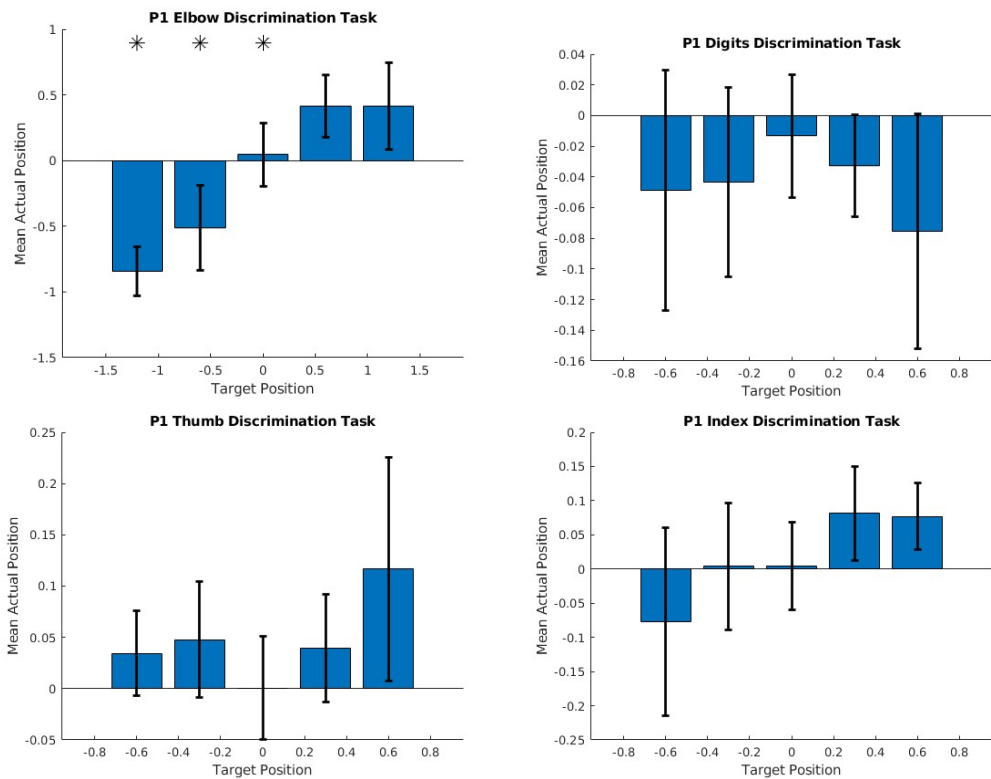


Figure 3-9: Mean virtual joint position based on target position tranche during graded control tasks. Bars that are significantly different from all others in that trial are marked with an asterisk. Error bars are symmetrically one standard deviation about the mean.

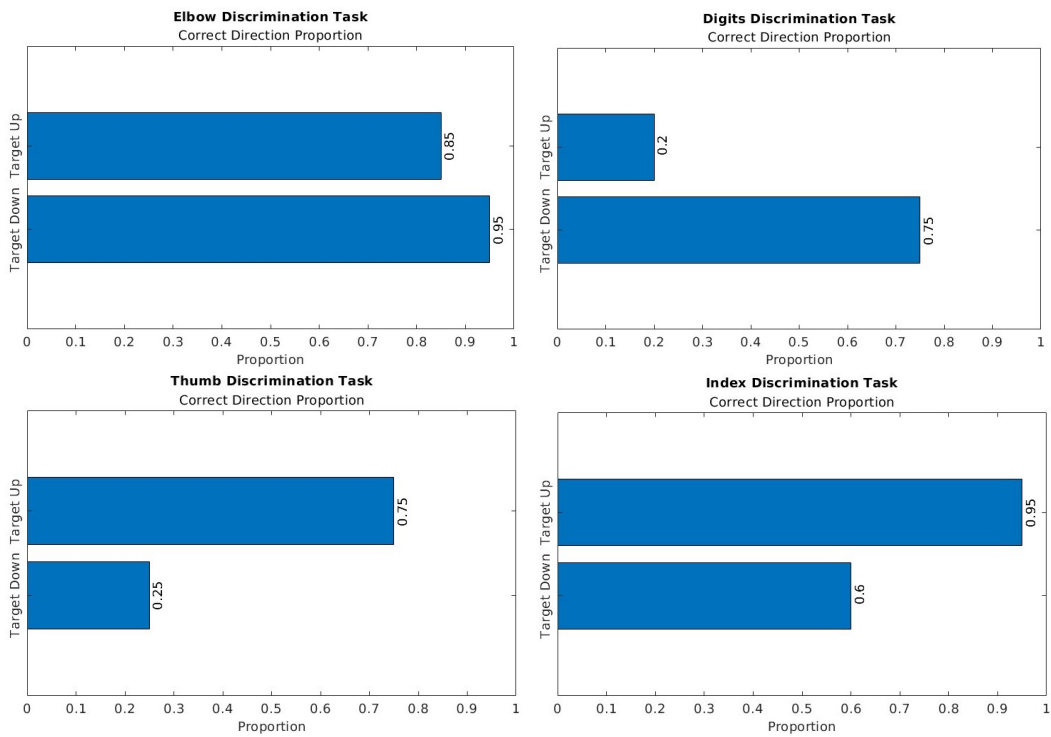


Figure 3-10: These bars show the fraction that the optimized model output moved in the same direction as the target position during the graded control tasks. 'Target Up' means that the target position was more flexed than the neutral position; 'Target Down' indicates that the target position was more extended than the neutral position

Table 3.6: Pairwise p -values for Differences between Model Outputs during Graded Control Tasks

	Tranche 2	Tranche 3	Tranche 4	Tranche 5
Elbow				
Tranche 1	0.0808*	$p < 1e-5^*$	$p < 1e-5^*$	$p < 1e-5^*$
Tranche 2	-	1.839e-4	$p < 1e-5^*$	1.734e-4*
Tranche 3	-	-	0.0558*	0.0521*
Tranche 4	-	-	-	0.9704
Digits				
Tranche 1	1	1	1	1
Tranche 2	-	1	1	1
Tranche 3	-	-	1	0.3312
Tranche 4	-	-	-	1
Thumb				
Tranche 1	1	1	1	0.1822
Tranche 2	-	0.6721	1	0.4592
Tranche 3	-	-	1	0.0029*
Tranche 4	-	-	-	0.2615
Index				
Tranche 1	0.5783	1	0.0043*	0.0060*
Tranche 2	-	1	0.7005	0.8752
Tranche 3	-	-	0.0944*	0.1248
Tranche 4	-	-	-	1

THIS PAGE INTENTIONALLY LEFT BLANK

Chapter 4

Discussion

4.1 Benefits of Biophysical Controllers

Existing control paradigms are unable to keep up with the demands of prosthesis users. Body-powered limbs are awkward to use and have low functionality, while commercially available myoelectric limbs use grip or velocity controllers. Most often, only a single degree of freedom can be controlled at a time and muscle co-contraction or an external device is needed to switch between them. In either case, the user has to focus on the movement of the prosthesis the entire time it is moving. This greatly increases the cognitive burden of using a prosthetic device [46]. It would be almost impossible to complete the graded control tasks as done in this work on a prosthesis using a grip controller and pattern recognition in the absence of visual feedback.

In [47], Roche et. al discuss a system that achieves 85% classification accuracy offline but leads to only a 55% movement completion rate during an assessment of prosthesis usability. Thus, high classification accuracy does not directly translate into dexterous control; for performance-critical tasks, such completion rates may be unacceptable. When considered along with the discomfort of socket and harness mounting systems, it is unsurprising that the estimated rate of prosthetic abandonment is over 50%, as covered in [2].

A biophysical model, on the other hand, is meant to mimic natural biomechanics. A position controlled model, such as the one developed in this work, can grant

more intuitive control over a prosthesis. In [27], it is theorized that motion planning occurs in task coordinates and not in joint coordinates, so a control scheme where a user thinks in movements could lead to more functional control. Due to the unique structure of the AMI, near-biological muscle strains are seen following amputation. Pairing the preservation of proprioception from the AMI with a position controller allows afferent neural feedback to close the control loop, such that a user does not have to watch their prosthesis to control it. When thinking in movements, muscles will fire according to stereotyped muscle synergies. Then a small number of muscles, with varied activation patterns, can be used to control a greater number of degrees of freedom than a 'one muscle pulls on one bone' understanding would suggest. This is how a four joint arm model was constructed from the subject with only two AMI constructs. The subjective sensation of AMI recipients, who often claim ownership over their synthetic limbs, is a powerful demonstration of how proprioception improves prosthetic embodiment and natural control [23].

4.2 Validity of the Simplified Model

Whenever a model is used, design choices need to be justified. In this thesis, a simplified model of the arm is used to map muscle excitation from the residual limb of a person with amputation to their intentions. Electromyography is the best available measure of muscle activation, though it is imperfect at that; with surface electrodes, the true signal is in practice low-pass filtered through soft tissue and skin. The EMG processing procedure also relies on filtering and approximations of muscle activation/deactivation dynamics, which further removes the iEMG signal from the motor intention vis-à-vis neural activation. Even worse, the same motion can be generated with different EMG patterns based on the limb configuration - this was demonstrated by Hogan [48]. Therefore, EMG by itself is insufficient as a measure of muscle force, though at low activation levels the relationship is nearly linear. When combined with optimization and pattern recognition techniques, or through synergy analysis, the activity of multiple muscles together provides a stronger signal of intended movement.

This is why a pattern recognition layer was applied between the processed iEMG and the muscle models to more accurately capture the subject's intentions.

The next consideration is the specific muscle representation chosen for the model. The Shadmher-Arbib model was used, with linear springs representing the elasticity of the muscle and tendon. As covered in 1.4.2, the passive muscle force-length and tendon force-length relationships are not linear in biological muscle-tendon units; is it valid to use this linear model? The parallel elastic element in this model only develops force when the muscle is stretched beyond its optimal length, as in the biological tissue. With an appropriate spring constant that approximates the average slope of this force-length relationship, a linear model can perform adequately to simulate the muscle. Similarly, an appropriate constant for the series elastic element can represent the average elongation of the tendon under load. At low strains, both of these approximations will overestimate the force in the muscle, but in effect this acts as a feedback signal that pulls the muscle back towards its rest length. The muscle model may then not often reach the lengths where the true normalized force-length values are higher than the approximation. As these are exponential relationships, this value can grow sharply; on average, the underestimate at higher strains and overestimate at lower strains may be approximately equal, such that over the course of a full trajectory, the movement of the model joint shows similar behavior to a biological joint. Additional modeling would be needed to assess the accuracy of the fit of the linear approximation.

In addition, the Shadmehr-Arbib model does not prescribe an active force-length curve shape and only states that the active force is a function of muscle length and activation. The Gaussian relationship employed by Thelen, with $\gamma = 0.45$, was chosen for this work as it closely matches the shape of the force-length curve in individual sarcomeres [15]. A shortcoming of this model is the linear viscous damping; this single parameter is insufficient to replicate the hyperbolic shape of the muscle force-velocity relationship, especially when the normalized force is greater than unity during muscle lengthening. Thus, the overall individual muscle model does have an active force-length, passive force-length, and tendon force-length relationship arguably sim-

ilar to that found in native muscles, though the force-velocity relationship is poorly represented.

An advantage of this model is that it does retain the linear force-stiffness behavior observed in skeletal muscle [16]. Therefore, when two such muscles are arranged about a single joint, the position and stiffness about that joint can be independently controlled using this model. It has been shown that modulating impedance is an important part of interacting with the environment [49] [50], so a model that demonstrates this behavior is well suited for deployment with advanced robotic upper extremity prostheses, which are designed for this behavior.

The Shadmehr-Arbib model is based on an areflexive muscle, which shows a linear force-stiffness relationship. This relationship changes when the stretch reflex is involved so that stiffness remains more flat over a wider range of muscle forces. It may seem odd to use an areflexive model in a controller for a prosthetic limb, especially given that the AMI is meant to retain afferent neural signaling post-amputation. The stretch reflex occurs following a sudden passive stretch in a muscle, often through the application of an external load. In an AMI recipient, the passive stretch cannot be applied as the limb segment that usually acts as a lever arm is gone. Therefore, it is justifiable to use an areflexive muscle in this model, especially given that this model has other desired properties.

4.3 Optimal Muscle Parameters

Further insight into the usefulness of this model is gained by considering the optimal parameter values. With symmetrical muscle attachments and assumed-symmetrical movement about the neutral point for each joint, it may be expected that the resulting optimal parameters would be nearly equal for the two muscles at each joint. This pattern is observed for some decision variables, though not for others. In an ideal case this may be a negative result, but the activation patterns must be considered as well. Looking at the first four channels of input iEMG during elbow flexion and extension in Figure 2-2, there is coactivation between both muscles in the AMI pair.

If both muscles are active during extension, the triceps muscle would have to be capable of producing more force than the biceps in order for the joint to extend. Thus, coactivation patterns influence the symmetry of some optimal parameters in the virtual muscles at each joint.

More specifically, the optimal lengths, maximal isometric forces, and series elastic constant were within 10% of each other for all antagonist muscle pairs. The optimal length and maximal isometric force define the behavior of the contractile element in the muscle. The larger the maximal force, the more force the muscle can generate for a given activation level. This force has to be transmitted through the tendon, represented by the series elastic spring. A stiffer spring deforms less under tension, such that the limb must move farther when the contractile element shortens a given distance. These factors increase the torque the muscle can generate and therefore can speed up the response of the joint. The optimal lengths, on the other hand, are near their upper bound for all muscles, so that the muscles are always on the ascending leg of the active force-length curve and generating less force than they otherwise could during all simulations with this model. Interestingly, these two effects seem to work against each other. Without further modeling, possibly considering wider parameter ranges or changing the fixed geometry of the joints, nothing firm can be said about this behavior. The convergence of these parameters near their maxima suggest that the performance of the system could be improved with different bounds, but these bounds may be less physiologically meaningful. As in all modeling, there are trade-offs between accuracy and performance.

Other parameters stay within the middle or towards the bottom of their ranges. The exact values taken on are less important than the relationships between them. The parallel elastic spring constants are significantly different than the series elastic spring constants for all muscles, which is to be expected: muscle tissue is much less stiff than tendons (hundreds of kPa compared to roughly 1 GPa, [43]). The low joint damping constants are also physiologically meaningful, as the synovial joints in the elbow and hand are lubricated to have low friction.

The final EMG weighting matrix is informative. Opposite signed coefficients for

the same channel on antagonist muscles are seen throughout Table 3.2. Again, in the ideal case these values would be negatives of each other so that high activation of one muscle is associated with little to no activity on the other muscle. Due to coactivation and crosstalk over the skin's surface, this pattern is not always seen. The matrix also shows that redundant channels over a given muscle do not always have the same weight. This could indicate that the electrodes are placed over different motor units and are picking up meaningfully different activations during movement, which would support the use of such a matrix as a pattern recognition layer. Alternatively, it could mean that the optimizer moved away from realistic virtual muscles and was overfitting the model to the data. Further modeling, likely with intramuscular needle electrodes, would be needed to separate these effects.

The optimized joints could quite effectively reproduce the input trajectories for most of the degrees of freedom. The calculated correlation between input and output were very high and the amplitudes of the optimized trajectories matched that of their references, demonstrating that such a model can reproduce smooth movements. This is further supported by the calculated dimensionless log jerks (DLJ), which are of roughly the same magnitude for input and output trajectories. It's important to note that these are log values, so a small difference in raw value can correspond to a large difference in total jerk over the trajectory. This is a meaningful difference because the model-generated trajectories are visually much less smooth than the references. However, DLJ normalizes by the squared peak velocity, which is notably higher in the model output trajectories.

The elbow is the best performing joint overall. Seeing as the muscles that move the physiological elbow were constructed into their own AMI pair, near-native activation patterns should be preserved and this virtual joint should benefit from this behavior. The optimized thumb performs the worst, which is supported by the iEMG activation patterns for the channels over the AMI for the hand muscles and the comments of subject P1. No clear peaks and troughs, corresponding to adduction and abduction of the thumb, are seen, making it hard to accurately recreate the reference trajectory or set EMG weights well. This does show the limitations of trying to build a model

with more degrees of freedom than there are agonist-antagonist pairs, as pattern recognition can only identify so many patterns with a given number of channels.

The impulse responses for each muscle demonstrate heavily damped to over-damped joint behavior. Though the damping of the joints themselves are low, the muscles act as dampers when they are stretched past their rest lengths. The peaks were reached on the order of 50 to 100 ms after the impulse, which is close to the behavior observed in biological muscles [25]. As stated above, the parameters for antagonist muscles were not always equal. The implications are seen in the impulse responses - subject to the same relative magnitude impulse, the peak joint displacements are not the same.

4.4 Replication of Native Biomechanics

4.4.1 Speed-Accuracy Tradeoff

Fitts' Law holds strong predictive power for human movement across many different regimes of movement. Testing of the model on movements of different frequencies is an important demonstration of how generalizable the results of an optimization can be. Given that the target distance was always the same, as the movement frequency increases and movement time goes down, the index of difficulty would have to increase for Fitts' Law to hold. Based on the Crossman formulation, the effective width must increase for the index of difficulty to increase. A higher effective width comes from a higher standard deviation of actual peak distance, which captures the speed-accuracy tradeoff. From the model-generated trajectories, this pattern is observed more in some joints than others. The elbow continues to perform the best, clearly oscillating at three different frequencies. Figure 3-3 shows the dominant frequencies, which are close to the desired frequencies of 0.25 Hz, 0.33 Hz, and 0.42 Hz, respectively. Nicely, the difference between the desired frequency and the actual frequency increases with movement speed, adhering to Fitts' Law and showing the speed-accuracy tradeoff.

Very little oscillation is observed in certain tests; this could be an indicator of low

quality input data as much as an indicator of model quality. Repeating these tests with additional subjects or in a point-to-point rather than continuous manner would allow finer calculations of the indices of difficulty and performance and separation of model inaccuracies from data inconsistencies. The amplitude of the oscillations was not the same for all trials. If the intended movements were through the full range of motion in the joint, and the model trajectories were not, there may be bandwidth limitations for the biophysical model not seen in the biological limb. A true Fitts' Law test sweeping many more frequencies would be needed to tell if these limitations are general or a consequence of the specific data collected during the trials. That said, the positive slopes on the regression lines between index of difficulty and movement time shows that this model is sufficient to replicate another repeatedly observed characteristic of volitional human motor control.

4.4.2 Graded Control Tasks

The graded control tasks were included to assess whether the model is actually moving according to the subject's intent or if the optimized model could only do bang-bang control between the maximum and minimum of the range of motion. An optimized muscle model that can move through full joint ranges of motion can illuminates some attributes of muscle physiology, like the magnitude difference in muscle and tendon elasticity. The bounds on these decision variables for optimization were the same, but the resulting values were very different, suggesting that there is something fundamental about the mechanism of force production in skeletal muscles that requires this difference. It could be that these viscoelasticities are 'just so'. Instead, seeing this result arise empirically means this more likely indicates a characteristic of real muscles. One likely explanation arises from the different makeup of muscle tissue and tendons; for sarcomeres to be able to contract, the protein filaments making them up must slide past each other and thus they cannot be extremely rigid, while the arrangement of parallel collagen fibers in tendons make them much stiffer.

Activities of daily living are not cyclical, and fine motor control is even less so. A model that cannot produce small motions and moves only at a fixed amplitude

is no better than a velocity controller. Presenting the target positions in a random order also ensures that the model can move to and from any point in the range of motion and not just cyclically, as all prior tests involved cyclical motion. These tests have been used to demonstrate a unique strength of the AMI construct. By restoring proprioception, the subject is better able to feel the stretch on their antagonist muscles during a volitional contraction that can signify the approximate position the biological limb would be with that level of activation. Preliminary evidence has shown that this allows the positioning of the virtual or phantom joints in space consistently in the absence of other feedback (visual or via functional electrical stimulation, as in [23]). As the graded control tasks for this work were completed without visual feedback, they are a test of both the AMI construct and the optimized model. Overall performance on these tasks was weak, suggesting that the model should be refined to produce graded outputs more accurately. For example, rather than using reference trajectories that go through the full joint range of motion, the subjects should do both a frequency and amplitude sweep so that a wider array of muscle activation patterns could be captured and used for model generation.

Only the elbow was able to consistently perform well through the entire 120 second trial, with 4 significantly different positions reached at the $\alpha = 0.1$ level. For a coarser analysis of graded control, the bar graphs in Figure 3-10 show simply how often the model output matched the target direction. These results were stronger, with most joints moving in the correct direction the majority of the time. As always, some of the optimized joints behaved pathologically, often moving in the entirely wrong direction. With refinements to the model allowing graded control, this style of optimized model could greatly improve the experiences of persons with amputation by decreasing the cognitive burden of prosthesis use. The ability to generate graded proportional control signals allows the user to think in actions rather than focusing on moving the arm and then stopping the arm when it reaches the desired position.

4.5 Contributions

This thesis presents methods for creating and validating subject-specific biophysical controllers for prosthetic arms based on their ability to emulate observed characteristics of human motor control. In particular, preliminary evidence from this work supports the following:

- Simplified models of the upper extremity leveraging single virtual muscle pairs as actuators for each degree of freedom can competently replicate reference trajectories given estimated muscle activation.
- As muscle strains in AMI constructs can correspond to the strains of virtual muscles, and proprioceptive feedback is known to improve prosthesis control, models of this type are well suited as prosthesis controllers for persons with AMI amputation.
- Neuromuscular models of this type are general enough to simulate movement patterns outside the motions used for optimization and are capable of demonstrating the speed-accuracy tradeoff as quantified by Fitts' Law.
- This biophysical model allows some degree of proportional control, though performance on these tasks is weak and suggests areas for improvement.

4.6 Future Directions

Though this model shows promise, more work is needed to replicate native biomechanics with a prosthetic arm. Of course, these methods should be explored with a larger pool of subjects with different numbers of AMI constructs and amputation levels to test how the techniques generalize. At the time of writing, four total subjects have undergone upper extremity amputation with AMIs constructed in their residual limbs; since the procedure is experimental, they have had to be generally healthy. With wider adoption, the variability in recipient morphology will grow and the amount of

data collected increases. Big data can improve patient-specific prosthesis controllers, like it has improved outcomes in other fields.

Many of the choices made during the model design could have been made differently, with their associated tradeoffs, and are worth exploring. For example, the constraints on the EMG matrix could be changed. The simple bound constraints were chosen because they are much easier for the optimizer to compute and enforce than equality or nonlinear constraints, but they are less restrictive, such that the results may signal coincidence rather than underlying phenomena. One such option is to use non-negative matrix factorization (NNMF) to do dimensionality reduction on the input iEMG, with the size of the factors a decision variable. This would be extremely computationally expensive, but if the results of such a model were strong, they could justify a longer setup period.

One obvious direction to take this work is to substitute the Shadmehr-Arbib model for an alternative mathematical model of muscle, such as the Thelen model. These models involve more parameters, but as computational power increases, multiple degree of freedom, highly motile and customized arm models can be designed according to the unique residual limb physiology of a person with amputation. Finally, all optimization work in this thesis was performed offline with data collected during very specific tasks. The development on an online training algorithm that continually updates as the user goes through their day-to-day activities would expand access to advanced position controllers; at present, they are only available in a select few biomechanics labs at leading institutions.

Imagining farther beyond the scope of this work, one can consider truly revolutionary advances in prosthetic limb technology. Myoelectric prostheses move with biologically-generated inputs, but as discussed above, they are not intuitively used. Neural signals can drive the devices, but not usually in a physiologically relevant manner. If proprioception proves to be the key to natural control of prosthetic devices without long habituation, generating afferent neural signals when a prosthetic interacts with the environment would further increase the functionality and embodiment of artificial limbs. If pressure sensors in the pads of the fingers of a robotic hand were

used to calculate the deflection of a joint while grasping an object, electrodes could stimulate contraction of one muscle in an AMI pair to produce antagonist strains and associated afferents corresponding to that joint deflection. The development of additional peripheral nerve interfaces for sensory feedback would further increase embodiment as well. In contrast to the neurally *controlled* prostheses of today, we will see completely neurally *integrated* prostheses within my lifetime.

Appendix A

Supplementary Figures

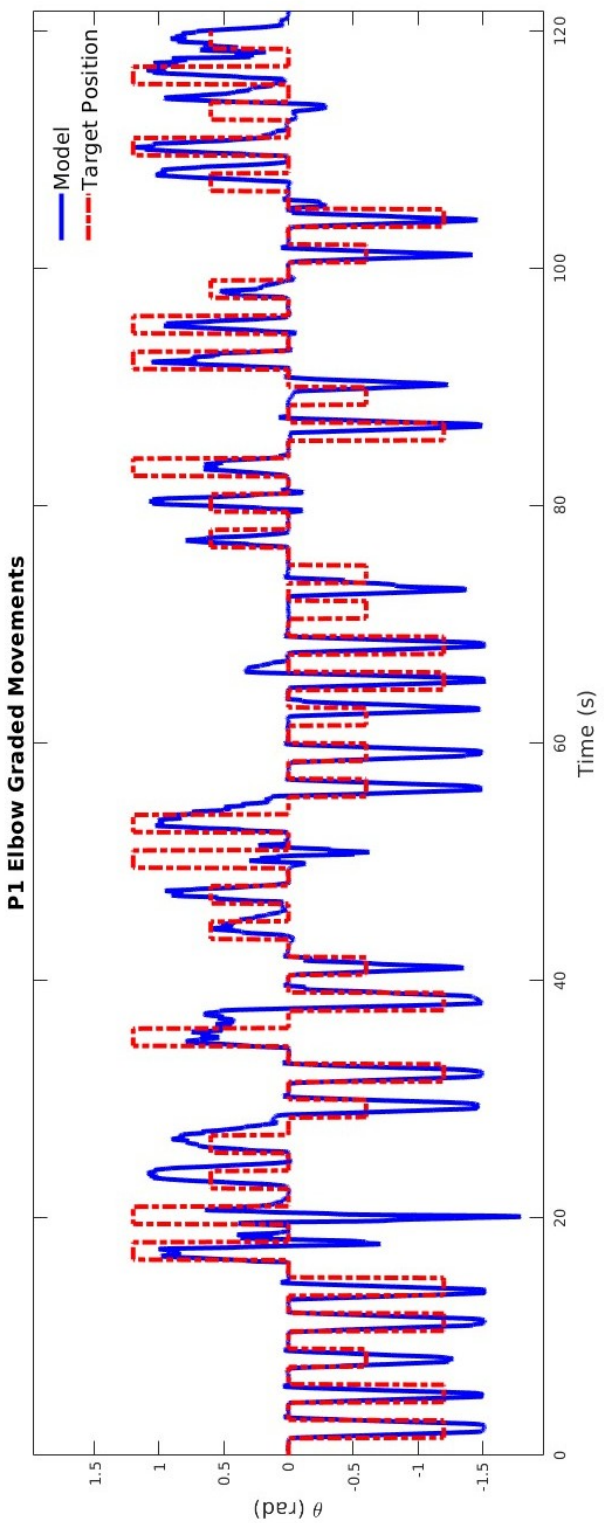


Figure A-1: Optimized model trajectory generated from sEMG collected during elbow graded control task overlaid on the target position

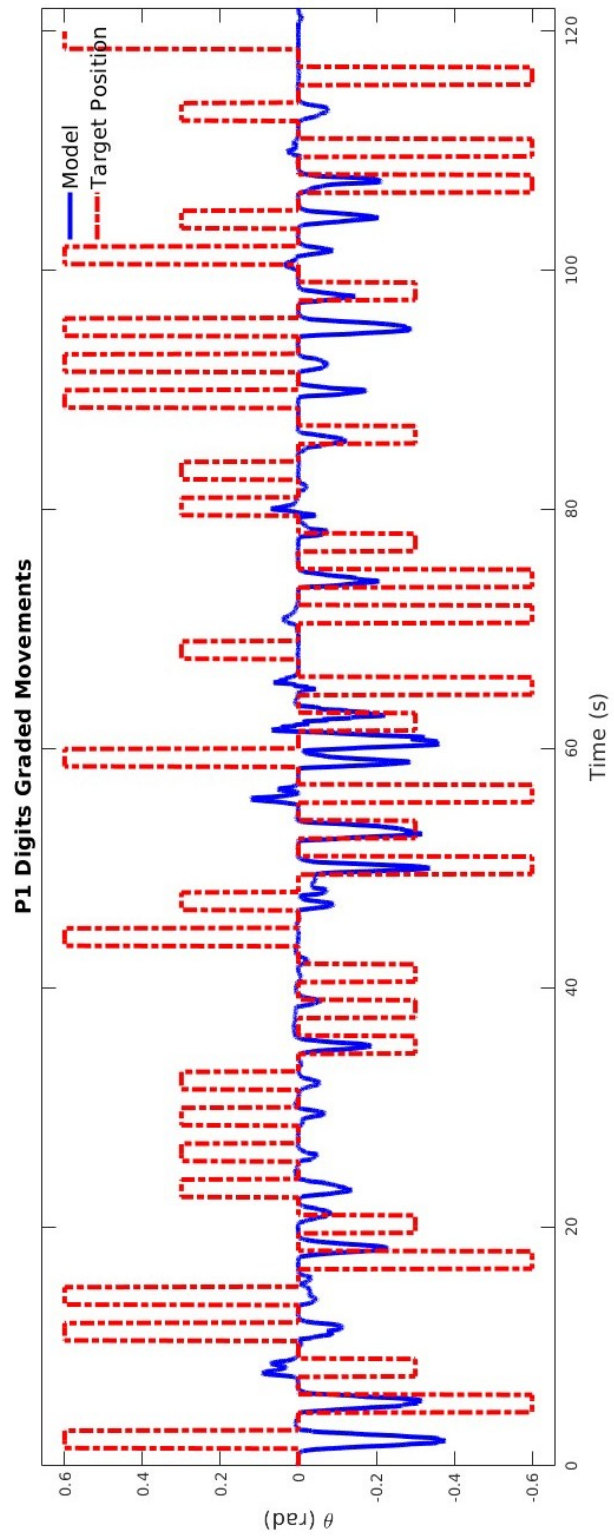


Figure A-2: Optimized model trajectory generated from sEMG collected during digits graded control task overlaid on the target position

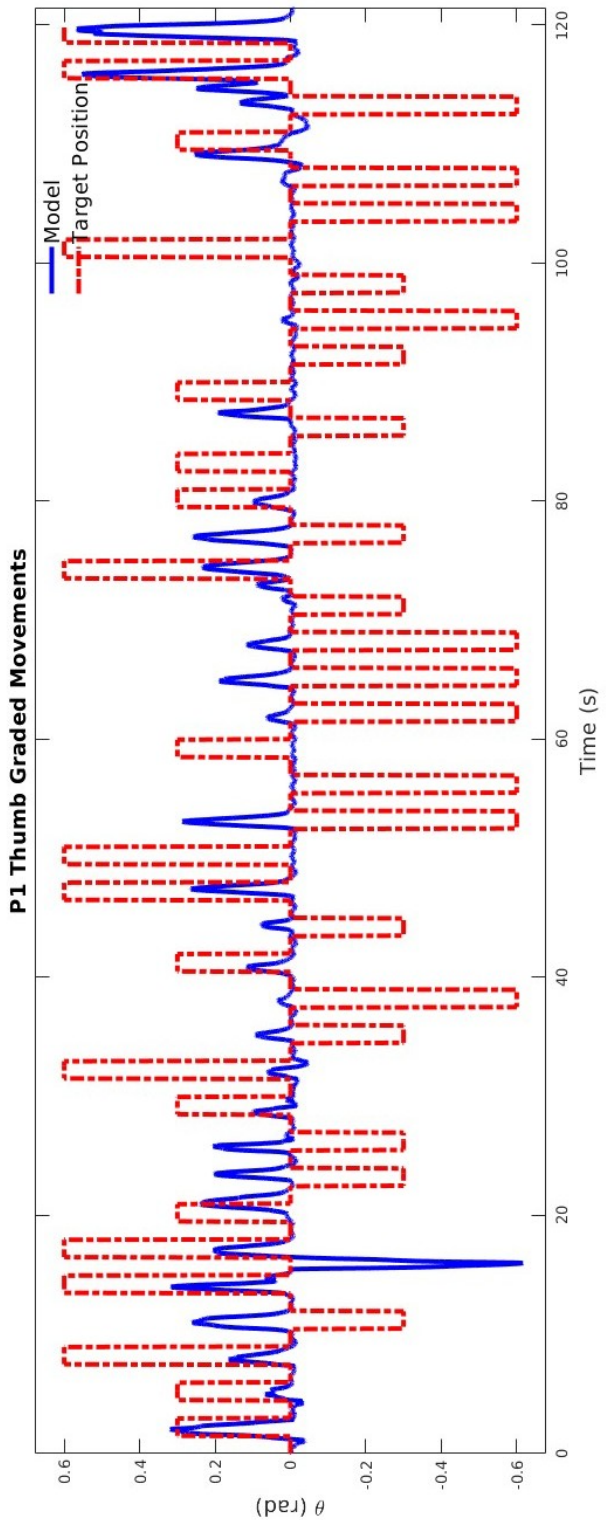


Figure A-3: Optimized model trajectory generated from sEMG collected during thumb graded control task overlaid on the target position

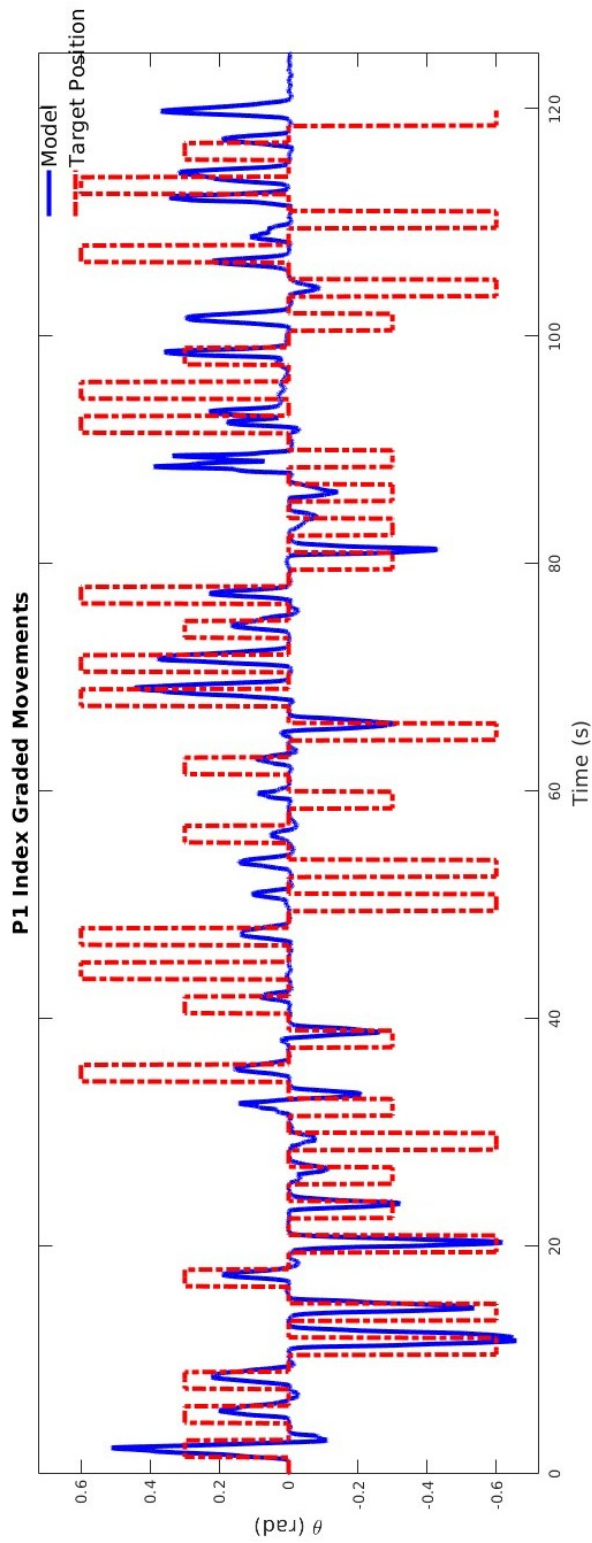


Figure A-4: Optimized model trajectory generated from sEMG collected during index graded control task overlaid on the target position

THIS PAGE INTENTIONALLY LEFT BLANK

Bibliography

- [1] Matthew S Johannes, John D Bigelow, James M Burck, Stuart D Harshbarger, Matthew V Kozlowski, and Thomas Van Doren. An Overview of the Developmental Process for the Modular Prosthetic Limb. *JOHNS HOPKINS APL TECHNICAL DIGEST*, 30(3):10, 2011.
- [2] Monica Espinosa and Dan Nathan-Roberts. Understanding Prosthetic Abandonment. *Proceedings of the Human Factors and Ergonomics Society Annual Meeting*, 63(1):1644–1648, November 2019. Publisher: SAGE Publications Inc.
- [3] W. W. Sutherling, M. F. Levesque, and C. Baumgartner. Cortical sensory representation of the human hand: size of finger regions and nonoverlapping digit somatotopy. *Neurology*, 42(5):1020–1028, May 1992.
- [4] muscles of the upper arm; human muscle system. Encyclopædia Britannica. <https://www.britannica.com/science/human-muscle-system/images-videos/media/1/1346474/119224>.
- [5] muscles of the human forearm. Encyclopædia Britannica. <https://www.britannica.com/science/human-muscle-system/images-videos/media/1/1346474/111229>.
- [6] muscles of the forearm; human muscle system. Encyclopædia Britannica. <https://www.britannica.com/science/human-muscle-system/images-videos/media/1/1346474/121138>.
- [7] Intrinsic muscles of the hand. Open Educational Resource (OER) - Unsyiah Library. <http://uilis.unsyiah.ac.id/oer/items/show/1153>.
- [8] Prathusha Maduri and Hossein Akhondi. *Upper Limb Amputation*. StatPearls Publishing, January 2022. Publication Title: StatPearls [Internet].
- [9] Kevin Cleveland. Amputations of the Upper Extremity.
- [10] Fatemeh Yavari, Farzad Towhidkhah, Mohammad-Ali Ahmadi-Pajouh, and Mohammad Darainy. The role of internal forward models and proprioception in hand position estimation. *J Integr Neurosci*, 14(3):403–418, September 2015.
- [11] Neville Hogan and Dagmar Sternad. Dynamic primitives of motor behavior. *Biol Cybern*, 106(11-12):727–739, December 2012.

- [12] Dr Jean Hanson and Dr Hugh E Huxley. STRUCTURAL BASIS OF THE CROSS-STRIATIONS IN MUSCLE. page 3, 1953.
- [13] David Richfield. Medical gallery of david richfield. WikiJournal of Medicine. DOI:10.15347/wjm/2014.009.
- [14] A.V. Hill. The heat of shortening and the dynamic constants of muscle. August 1938.
- [15] Darryl G. Thelen. Adjustment of muscle mechanics model parameters to simulate dynamic contractions in older adults. *J Biomech Eng*, 125(1):70–77, February 2003.
- [16] R. Shadmehr and M. A. Arbib. A mathematical analysis of the force-stiffness characteristics of muscles in control of a single joint system. *Biol Cybern*, 66(6):463–477, 1992.
- [17] Kim E. Barrett, Susan M. Barman, Heddwen L. Brooks, and Jason X.-J. Yuan. *Excitable Tissue: Muscle*. McGraw-Hill Education, New York, NY, 2019.
- [18] Henry Vandyke Carter. Organ of golgi (neurotendinous spindle) from the human tendo calcaneus. Anatomy of the Human Body.
- [19] Arthur J. van Soest and Maarten F. Bobbert. The contribution of muscle properties in the control of explosive movements. *Biol. Cybern.*, 69(3):195–204, July 1993.
- [20] M Silva. *Human motion analysis using multibody dynamics and optimization tools*. PhD thesis, Instituto Superior Técnico, Universidade Técnica de Lisboa, 2003.
- [21] Thang Tien Nguyen, Holly Warner, Hung La, Hanieh Mohammadi, Dan Simon, and Hanz Richter. State Estimation For An Agonistic-Antagonistic Muscle System. *Asian Journal of Control*, 21(1):354–363, January 2019.
- [22] Tyler R. Clites, Matthew J. Carty, Shriya Srinivasan, Anthony N. Zorzos, and Hugh M. Herr. A murine model of a novel surgical architecture for proprioceptive muscle feedback and its potential application to control of advanced limb prostheses. *J. Neural Eng.*, 14(3):036002, March 2017. Publisher: IOP Publishing.
- [23] Tyler R. Clites, Matthew J. Carty, Jessica B. Ullauri, Matthew E. Carney, Luke M. Mooney, Jean-François Duval, Shriya S. Srinivasan, and Hugh. M. Herr. Proprioception from a neurally controlled lower-extremity prosthesis. *Science Translational Medicine*, 10(443):eaap8373, May 2018. Publisher: American Association for the Advancement of Science.
- [24] Tyler R. Clites, Hugh M. Herr, Shriya S. Srinivasan, Anthony N. Zorzos, and Matthew J. Carty. The Ewing Amputation: The First Human Implementation of the Agonist-Antagonist Myoneural Interface. *Plastic and Reconstructive Surgery – Global Open*, 6(11):e1997, November 2018.

- [25] J. P. van Zandwijk, M. F. Bobbert, J. Harlaar, and A. L. Hof. From twitch to tetanus for human muscle: experimental data and model predictions for m. triceps surae. *Biological Cybernetics*, 79(2):121–130, August 1998.
- [26] P. Morasso. Spatial control of arm movements. *Exp Brain Res*, 42(2):223–227, 1981.
- [27] T Flash and N Hogan. The coordination of arm movements: an experimentally confirmed mathematical model. *J. Neurosci.*, 5(7):1688–1703, July 1985.
- [28] J. R. Flanagan and A. K. Rao. Trajectory adaptation to a nonlinear visuomotor transformation: evidence of motion planning in visually perceived space. *J Neurophysiol*, 74(5):2174–2178, November 1995.
- [29] R. Shadmehr and F. A. Mussa-Ivaldi. Adaptive representation of dynamics during learning of a motor task. *J. Neurosci.*, 14(5):3208–3224, May 1994. Publisher: Society for Neuroscience Section: Articles.
- [30] A. J. Bastian, T. A. Martin, J. G. Keating, and W. T. Thach. Cerebellar ataxia: abnormal control of interaction torques across multiple joints. *J Neurophysiol*, 76(1):492–509, July 1996.
- [31] Paul M. Fitts. The information capacity of the human motor system in controlling the amplitude of movement. *Journal of Experimental Psychology*, 47(6):381. Publisher: US: American Psychological Association.
- [32] Zachary C. Thumser, Andrew B. Slifkin, Dylan T. Beckler, and Paul D. Marasco. Fitts’ Law in the Control of Isometric Grip Force With Naturalistic Targets. *Frontiers in Psychology*, 9, 2018.
- [33] ERROL R. HOFFMANN. A comparison of hand and foot movement times. *Ergonomics*, 34(4):397–406, April 1991. Publisher: Taylor & Francis _eprint: <https://doi.org/10.1080/00140139108967324>.
- [34] A Comparison of Input Devices in Elemental Pointing and Dragging Tasks.
- [35] Robert Kerr. Movement Time in an Underwater Environment. *Journal of Motor Behavior*, 5(3):175–178, September 1973. Publisher: Routledge _eprint: <https://doi.org/10.1080/00222895.1973.10734962>.
- [36] E. R. Crossman and P. J. Goodeve. Feedback control of hand-movement and Fitts’ Law. *Q J Exp Psychol A*, 35(Pt 2):251–278, May 1983.
- [37] Ernest N. Kamavuako, Erik J. Scheme, and Kevin B. Englehart. On the usability of intramuscular EMG for prosthetic control: A Fitts’ Law approach. *Journal of Electromyography and Kinesiology*, 24(5):770–777, October 2014.

- [38] Sophie M. Wurth and Levi J. Hargrove. A real-time comparison between direct control, sequential pattern recognition control and simultaneous pattern recognition control using a Fitts' law style assessment procedure. *Journal of NeuroEngineering and Rehabilitation*, 11(1):91, May 2014.
- [39] Todd A Kuiken, Guanglin Li, Blair A Lock, Robert D Lipschutz, Laura A Miller, Kathy A Stubblefield, and Kevin B Englehart. Targeted Muscle Reinnervation for Real-time Myoelectric Control of Multifunction Artificial Arms. page 10.
- [40] Thomas S. Buchanan, David G. Lloyd, Kurt Manal, and Thor F. Besier. Neuromusculoskeletal Modeling: Estimation of Muscle Forces and Joint Moments and Movements From Measurements of Neural Command. *J Appl Biomech*, 20(4):367–395, November 2004.
- [41] Rudolfs Drillis. A Survey of Measurement Techniques. page 23.
- [42] Xiao Hu, Wendy M. Murray, and Eric J. Perreault. Muscle short-range stiffness can be used to estimate the endpoint stiffness of the human arm. *J Neurophysiol*, 105(4):1633–1641, April 2011.
- [43] F. E. Zajac. Muscle and tendon: properties, models, scaling, and application to biomechanics and motor control. *Crit Rev Biomed Eng*, 17(4):359–411, 1989.
- [44] Z.M. Li, V.M. Zatsiorsky, and M.L. Latash. Contribution of the extrinsic and intrinsic hand muscles to the moments in finger joints. *Clinical Biomechanics*, 15(3):203–211, March 2000.
- [45] Michael A. Sherman, Ajay Seth, and Scott L. Delp. WHAT IS A MOMENT ARM? CALCULATING MUSCLE EFFECTIVENESS IN BIOMECHANICAL MODELS USING GENERALIZED COORDINATES. *Proc ASME Des Eng Tech Conf*, 2013:V07BT10A052, August 2013.
- [46] Saffran Möller, David Rusaw, Kerstin Hagberg, and Nerrollyn Ramstrand. Reduced cortical brain activity with the use of microprocessor-controlled prosthetic knees during walking. *Prosthet Orthot Int*, 43(3):257–265, June 2019.
- [47] Aidan D. Roche, Hubertus Rehbaum, Dario Farina, and Oskar C. Aszmann. Prosthetic Myoelectric Control Strategies: A Clinical Perspective. *Current Surgery Reports*, 2(3):44, January 2014.
- [48] N. Hogan. Adaptive control of mechanical impedance by coactivation of antagonist muscles. *IEEE Transactions on Automatic Control*, 29(8):681–690, August 1984. Conference Name: IEEE Transactions on Automatic Control.
- [49] J. McIntyre, F. A. Mussa-Ivaldi, and E. Bizzi. The control of stable postures in the multijoint arm. *Exp Brain Res*, 110(2):248–264, July 1996.
- [50] Akihiko Murai. Impedance model of the interaction between environment and human body and its modification design. *Annu Int Conf IEEE Eng Med Biol Soc*, July 2018.